# Dynamical Viability of Anisotropic Kaniadakis Holographic Dark Energy Models within Brans–Dicke–Rastall Gravity

Y. Aditya[1,a], U.Y. Divya Prasanthi[2,b], D. Ram Babu[1,c]
[1]Department of Mathematics, GMR Institute of Technology (GMRIT) – Deemed to be University, Rajam-532127, India
[2]Department of Statistics & Mathematics, College of Horticulture, Dr. Y.S.R. Horticultural University, Parvathipuram-535502, India
[a]aditya.y@gmrit.edu.in; [b]divyaaug24@gmail.com; [c]rambabuphd23@gmail.com;
(Submitted on 14.11.2025; Accepted on 24.01.2026)

**Abstract.** In this work, we explore the cosmological dynamics of Kaniadakis holographic dark energy within an anisotropic Bianchi type-I space-time in the framework of Brans–Dicke–Rastall gravity. By assuming a proportional relationship among the metric potentials and introducing a suitable connection between the Brans–Dicke scalar field and the average scale factor, we obtain an exact analytical solution describing the background evolution. The resulting cosmological model incorporates pressureless matter together with Kaniadakis holographic dark energy formulated using both the Hubble and Granda–Oliveros infrared cutoffs. Employing the latest cosmic chronometer and baryon acoustic oscillations observational datasets, we constrain the model parameters and examine the resulting dynamics. A comprehensive analysis is carried out, encompassing the behaviour of the Hubble and deceleration parameters, the equation of state, the statefinder hierarchy, the Om-diagnostic, the coincidence parameter, the squared sound speed, and thermodynamic quantities such as entropy density and temperature. Our findings show that the model exhibits phantom or quintom-like behaviour at early times and transitions smoothly toward a $\Lambda$CDM-like state at late epochs, with the Granda–Oliveros cutoff yielding superior dynamical stability compared to the Hubble cutoff. The squared sound speed and thermodynamic diagnostics confirm the classical and thermodynamic viability of the model, while the predicted cosmic age agrees well with Planck observations. Taken together, the analytical solutions and observational constraints demonstrate that Kaniadakis holographic dark energy in the Brans–Dicke–Rastall gravitational framework constitutes a physically consistent and observationally robust model for explaining the late-time acceleration of the Universe.

**Key words:** Kaniadakis holographic dark energy, Brans-Dicke-Rastall gravity, Bianchi type-$I$ universe, Anisotropic model, Cosmology.

## 1 Introduction

Contemporary astrophysical observations indicate that the present-day Universe is undergoing accelerated expansion driven by a mysterious form of energy with large negative pressure, known as dark energy (DE) (Perlmutter et al. 1998; Riess et al. 1998). Additional evidence from Cosmic Microwave Background (CMB) anisotropies measured by the Wilkinson Microwave Anisotropy Probe (WMAP) (Spergel et al. 2003) and Large-Scale Structure surveys (Verde et al. 2002) suggests that nearly two-thirds of the total cosmic energy density consists of DE, while the remainder is composed of relativistic dark matter and baryonic matter (Hinshaw et al. 2009). The physical nature of DE is commonly characterized by its equation of state (EoS) parameter $\omega$, defined as the ratio of pressure to energy density. Cosmic acceleration requires $\omega < -\frac{1}{3}$. Scalar-field models identify DE as quintessence when $-1 < \omega < -\frac{1}{3}$ (Zlatev et al. 1999; Steinhardt et al. 1999) and as phantom energy when $\omega < -1$ (Caldwell et al. 2003). Phantom energy is particularly noteworthy due to its ability to drive

the Universe toward a future finite-time singularity and its violation of the strong energy condition, which has implications for wormhole physics (Hassan et al. 2021). To address the DE problem, several alternative frameworks have been proposed. Inspired by black hole thermodynamics (Hawking 1975), 't Hooft introduced the holographic principle (Hooft 1993), which later led to the development of holographic DE (HDE) (Li 2004). Modified versions of HDE using different infrared (IR) cut-offs (e.g., Hubble and Granda–Oliveros (GO)) have been studied in (Chirde and Shekh 2018; Wang et al. 2017).

The holographic principle forms the foundation of HDE models, where the DE density is assumed to scale inversely with the square of a suitably chosen IR cutoff, $L^3\rho_{de} \leq M_p^2 L$ (where quantity $L$ is the infrared (IR) cut-off scale and $M_p^2 = \frac{1}{8\pi G}$ is the reduced Planck mass). This framework has been widely applied in cosmology, particularly for modeling the late-time acceleration through the HDE scenario (Li 2004; Wang et al. 2017; Pavon and Zimdahl 2005). Unlike conventional DE models that introduce additional dynamical fields or modify the gravitational action, the HDE model is derived directly from holographic considerations and dimensional analysis, rendering it conceptually distinct from traditional approaches. Beyond its relevance to the DE-dominated era, the holographic principle has also been employed to describe the early inflationary phase of the Universe (Nojiri et al. 2019). In the early epoch, the smallness of the scale factor leads to a large holographic energy density, sufficient to drive accelerated expansion. Such holographic inflationary models are compatible with the 2018 Planck observations. More recently, Nojiri et al. (2020) demonstrated that holographic energy density can consistently unify both early-time inflation and late-time DE within a covariant theoretical framework. In their earlier work, Nojiri and Odintsov (2006) also developed a unified description of cosmic acceleration within the context of phantom cosmology. Subsequently, Nojiri et al. (2021) explored a broad class of DE models that can be understood as members of a generalized HDE family, each specified by a characteristic IR cutoff. Moreover, Nojiri et al. (2022a) emphasized that while the Bekenstein–Hawking entropy is central to horizon thermodynamics, it can receive quantum and non-extensive corrections. Such modified entropy frameworks, when applied to black hole physics and HDE models, have been shown to drive early-time inflation and may even alleviate the present Hubble tension. Recent developments have introduced generalized entropy formalisms—such as Tsallis (Tsallis and Cirto 2013), Sharma–Mittal (Jahromi et al. 2018), and Rényi (Moradpour et al. 2018)—to construct extended HDE models (Prasanthi and Aditya 2021). A significant advancement in this direction was made by Nojiri et al. (2022b, 2024), who proposed a four-parameter generalized entropy function encompassing several known entropy measures—including Tsallis, Rényi, Barrow, Sharma–Mittal, Kaniadakis, and loop quantum gravity-inspired entropies—as special limiting cases. Their analysis showed that this generalized entropy can yield a unified entropic cosmology capable of describing both the early inflationary epoch and the late-time DE-dominated phase. Among the various generalized entropies, the Kaniadakis entropy (or $\mathcal{K}$-entropy) introduced by Kaniadakis (2001) stands out as an elegant one-parameter deformation of the Boltzmann–Gibbs entropy, characterized by the deformation parameter $\mathcal{K}$.

This statistical framework naturally captures deviations relevant in extreme gravitational or cosmological environments (Masi 2005; Abreu et al. 2018). Incorporating $\mathcal{K}$-entropy into the HDE framework leads to the Kaniadakis HDE (KHDE) model (Moradpour et al. 2020), which provides additional flexibility in addressing long-standing issues such as cosmic coincidence and fine-tuning.

Another approach to explaining late-time cosmic acceleration is to modify the geometric sector of the Einstein–Hilbert action. Motivated by the inability of General Relativity (GR) to account for the observed acceleration, several extensions of Einstein's theory have been proposed (Copeland et al. 2006; Capozziello 2002; Joyce et al. 2015). While GR is formulated in a Riemannian spacetime with vanishing torsion and non-metricity, alternative formulations—such as teleparallel and metric-affine gravity—reinterpret gravitation through torsion or non-metricity, offering new geometric perspectives on cosmic dynamics. In GR, the covariant conservation of the energy–momentum tensor (EMT) is a central assumption, though lacking direct experimental verification. This has motivated theories in which the EMT is not strictly conserved. Rastall (1972) introduced one such modification, where the EMT divergence is proportional to the gradient of the Ricci scalar, implying a non-minimal coupling between matter and curvature (De Moraes and Santos 2019). Despite its simplicity, Rastall gravity produces rich cosmological behavior without introducing additional fields (Gibbons and Hawking 1977; Ford 1987; Batista et al. 2012), though its status as an extension of GR remains debated (Visser 2018). Recent studies continue to explore its dynamical implications (Singh, Singh and Pradhan 2022; Singh and Pradhan 2023). To incorporate a dynamical gravitational coupling, Rastall's framework has been extended with a scalar field, leading to the Brans–Dicke–Rastall (BDR) theory (Carames et al. 2014). This hybrid model combines the scalar–tensor dynamics of Brans–Dicke gravity (Brans and Dicke 1961) with Rastall's modified conservation law, yielding a richer phenomenology. In BDR theory, the scalar field $\phi$ evolves with cosmic time and interacts with curvature, allowing both the effective gravitational coupling and the matter–geometry relation to vary dynamically. This makes BDR a useful framework for exploring cosmic acceleration, anisotropic evolution, and DE dynamics.

In cosmology, the Friedmann–Lemaître–Robertson–Walker (FLRW) framework assumes perfect spatial isotropy on large scales. Yet, both theoretical considerations and observational indications suggest that the early Universe may not have been exactly isotropic. In this context, the Bianchi type-I (BT-I) geometry serves as the simplest anisotropic extension of the FLRW model. Its homogeneous but directionally dependent metric allows one to incorporate anisotropic effects without sacrificing overall spatial uniformity. This makes the BT-I space-time an effective arena for examining how directional anisotropies influence cosmic evolution. Accordingly, formulating KHDE models within the BT-I background provides a natural approach for probing the combined impact of anisotropy and quantum entropy corrections on the Universe's expansion dynamics. In recent times, several authors have explored different HDE models in anisotropic backgrounds and modified gravities separately (Prasanthi and Aditya 2020; Aditya and Reddy 2018a; Santhi and Chinnappalanaidu 2023; Aditya and Reddy 2018b; Aditya and Reddy 2018c; Aditya 2024). In particular, studies on KHDE are also emerging in various contexts

(Jawad and Sultan 2021; Sharma et al. 2022; Drepanou et al. 2022; Sadeghi et al. 2023; Rao et al. 2024; Prasanthi et al. 2024). Ghaffari (2022) studied the KHDE model in BD theory of gravity and investigated its cosmological consequences. Ali et al. (2024) explored the dynamics of the isotropic KHDE model in the Chern–Simons modified theory. Murali et al. (2024, 2025) and Aditya (2025) have investigated anisotropic KHDE models in scalar–tensor theory of gravity. From the above discussion, it is clear that the KHDE framework has been widely investigated across different gravitational theories and cosmological settings. However, to the best of our knowledge, the KHDE model has not yet been examined within a BT-I anisotropic universe under the BDR theory of gravity. This gap in the literature provides strong motivation for the present study, in which we analyze the cosmological behavior of KHDE by employing two choices of IR cutoffs – namely, the Hubble horizon and the GO cutoff.

In this work, we construct two anisotropic cosmological models within the KHDE framework: model-1 based on the Hubble horizon as the IR cutoff, and model-2 based on the GO cutoff. To assess their observational viability, we constrain the model parameters using recent cosmic chronometer (CC) data as well as the combined CC+Baryon Acoustic Oscillations (BAO) dataset. A Markov Chain Monte Carlo (MCMC) analysis is performed to extract the best-fit parameter values and their corresponding uncertainties. The structure of the paper is organized as follows: Section 2 presents the field equations of the BDR framework along with their analytical solutions. Section 3 provides the observational constraints using CC and CC+BAO datasets through MCMC analysis. In Section 4, we discuss the dynamical and physical behavior of the models. Finally, Section 5 summarizes our findings and outlines the main conclusions of the study.

## 2 Kaniadakis holographic dark energy models

In the Brans–Dicke (BD) framework, the gravitational coupling is treated as a dynamical quantity, given by $G = \frac{1}{\phi}$, where $\phi$ denotes the BD scalar field. Extending Rastall's hypothesis to the scalar–tensor regime and introducing the correspondence $\lambda_{\rm Ras} = \frac{3\lambda-2}{2\lambda-1}$, with $\lambda$ being the BDR parameter, the modified non-conservation law of the energy–momentum tensor becomes

$$T^{ij}_{\ ;i} = \frac{(1-\lambda)\phi}{16\pi} R^{,j}. \tag{1}$$

This relation illustrates that the divergence of the energy–momentum tensor is proportional to the gradient of the Ricci scalar, implying an exchange of energy between matter and geometry mediated by the scalar field $\phi$. Such a mechanism encapsulates the core philosophy of Rastall gravity, where standard conservation laws are relaxed in curved spacetime. Caramês et al. (2014) generalized Rastall's field equations to the BD scenario and obtained the modified field equations,

$$R_{ij} - \frac{\lambda}{2} g_{ij} R = \frac{8\pi}{\phi} T_{ij} + \left( -\frac{1}{2} g_{ij} \phi_{;k} \phi^{;k} + \phi_{;i} \phi_{;j} \right) \frac{w}{\phi^2} + \frac{1}{\phi} \left( -g_{ij} \Box \phi + \phi_{;i;j} \right), \tag{2}$$

where $w$ is the dimensionless BD coupling parameter and $\phi$ is the scalar field modulating the strength of gravity. Taking the trace of Eq. (2) yields

$$R = \frac{1}{1-2\lambda}\left(\frac{8\pi}{\phi}T - \frac{w}{\phi^2}\phi_{;k}\phi^{;k} - 3\frac{\Box\phi}{\phi}\right). \tag{3}$$

Substituting Eq. (3) back into Eq. (2) leads to the BDR field equations in the form

$$R_{ij} - \frac{1}{2}g_{ij}R = \frac{8\pi}{\phi}\left(T_{ij} - \frac{1-\lambda}{2(1-2\lambda)}g_{ij}T\right) + \left(\frac{\lambda}{2(1-2\lambda)}g_{ij}\phi_{;k}\phi^{;k} + \phi_{;i}\phi_{;j}\right)\frac{w}{\phi^2} + \frac{1}{\phi}\left(\frac{1+\lambda}{2(1-2\lambda)}g_{ij}\Box\phi + \phi_{;i;j}\right). \tag{4}$$

Applying the Bianchi identities to Eq. (4) gives the evolution equation for the scalar field,

$$\Box\phi = \frac{8\pi\lambda}{3\lambda - 2(1-2\lambda)w}T - \frac{w(1-\lambda)}{3\lambda - 2(1-2\lambda)w}\frac{\phi^{;k}\phi_{;k}}{\phi}. \tag{5}$$

Equation (5) governs the dynamics of the BD scalar field in the presence of a non-minimal interaction between matter and curvature. For $\lambda = 1$, the standard BD theory is recovered, reinstating the conservation of the energy–momentum tensor and reducing to GR in the appropriate limit.

We now consider the locally rotationally symmetric (LRS) BT-I metric expressed as

$$ds^2 = -dt^2 + A^2(t)\,dx^2 + B^2(t)\,(dy^2 + dz^2), \tag{6}$$

where the scale factors $A(t)$ and $B(t)$ depend solely on cosmic time $t$. The energy–momentum tensor of the cosmic fluid is assumed to be anisotropic and is decomposed as $T_{ij} = T^m_{ij} + T^{de}_{ij}$ with

$$\begin{aligned} T^m_{ij} &= \mathrm{diag}[0,0,0,1]\;\rho_m, \\ T^{de}_{ij} &= \mathrm{diag}[-(\omega_{de}+\xi), -\omega_{de}, -\omega_{de}, 1]\;\rho_{de}, \end{aligned} \tag{7}$$

where $\rho_m$ and $\rho_{de}$ denote the energy densities of matter and DE, respectively, while $\omega_{de}$ is the equation-of-state parameter of DE. The parameter $\xi$ quantifies the deviation in the pressure along the $x$- direction from the standard EoS.

Using the metric (6) and the energy–momentum components (7), the BDR field equations (4) in a comoving coordinate system can be expressed as

$$2\frac{\dot{A}}{A}\frac{\dot{B}}{B} + \left(\frac{\dot{B}}{B}\right)^2 = \frac{8\pi}{\phi}\left(\frac{1+\lambda}{2-4\lambda}\omega_{de}\rho_{de} + \frac{1-\lambda}{2-4\lambda}\xi\rho_{de} + \frac{\lambda-1}{2-4\lambda}(\rho_m + \rho_{de})\right) + w\left(\frac{\dot{\phi}}{\phi}\right)^2 \times\left(\frac{\lambda}{2-4\lambda}\right) + \left(\frac{2-\lambda}{1-2\lambda}\right)\frac{\dot{A}}{A}\frac{\dot{\phi}}{\phi} + \left(\frac{1+\lambda}{2-4\lambda}\right)\frac{\dot{C}}{C}\frac{\dot{\phi}}{\phi} + \left(\frac{1+\lambda}{2-4\lambda}\right)\frac{\ddot{\phi}}{\phi} \tag{8}$$

$$2\frac{\ddot{B}}{B}+\left(\frac{\dot{B}}{B}\right)^2=\frac{8\pi}{\phi}\left(\frac{1+\lambda}{2-4\lambda}\omega_{de}\rho_{de}+\frac{3\lambda-1}{2-4\lambda}\xi\rho_{de}+\frac{\lambda-1}{2-4\lambda}(\rho_m+\rho_{de})\right)+w\left(\frac{\dot{\phi}}{\phi}\right)^2 \times\left(\frac{\lambda}{2-4\lambda}\right)+\left(\frac{1+\lambda}{1-2\lambda}\right)\frac{\dot{A}}{A}\frac{\dot{\phi}}{\phi}+\left(\frac{3-3\lambda}{2-4\lambda}\right)\frac{\dot{C}}{C}\frac{\dot{\phi}}{\phi}+\left(\frac{1+\lambda}{2-4\lambda}\right)\frac{\ddot{\phi}}{\phi} \quad (9)$$

$$\frac{\ddot{A}}{A}+\frac{\ddot{B}}{B}+\frac{\dot{A}}{A}\frac{\dot{B}}{B}=\frac{8\pi}{\phi}\left(\frac{1-3\lambda}{2-4\lambda}(\rho_m+\rho_{de})+\frac{3-3\lambda}{2-4\lambda}\omega_{de}\rho_{de}+\frac{1-\lambda}{2-4\lambda}\xi\rho_{de}\right)+w\left(\frac{\dot{\phi}}{\phi}\right)^2 \times\left(\frac{2-3\lambda}{2-4\lambda}\right)+\left(\frac{1+\lambda}{1-2\lambda}\right)\frac{\dot{A}}{A}\frac{\dot{\phi}}{\phi}+\left(\frac{1+\lambda}{2-4\lambda}\right)\frac{\dot{C}}{C}\frac{\dot{\phi}}{\phi}+\left(\frac{3-3\lambda}{2-4\lambda}\right)\frac{\ddot{\phi}}{\phi} \quad (10)$$

$$\ddot{\phi}+\left(\frac{\dot{A}}{A}+2\frac{\dot{B}}{B}\right)\dot{\phi}=\left(\frac{8\pi\lambda(\rho_{de}+\rho_m-3\omega_{de}\rho_{de}-\xi\rho_{de})}{3\lambda-2(1-2\lambda)w}\right)-\left(\frac{w(1-\lambda)}{3\lambda-2(1-2\lambda)w}\right)\left(\frac{\dot{\phi}^2}{\phi}\right) \quad (11)$$

The field equations given in Eqs. (8)–(11) constitute a system of four independent relations involving six unknown quantities, namely the metric potentials $A$ and $B$, the energy densities $\rho_{de}$ and $\rho_m$, the DE equation-of-state parameter $\omega_{de}$, and the deviation parameter $\xi$. To obtain a deterministic solution, additional physically motivated conditions must be imposed. A widely used assumption in anisotropic cosmology is the proportionality between the expansion scalar $\theta=\frac{\dot{A}}{A}+2\frac{\dot{B}}{B}$ and the shear scalar $\sigma^2=\frac{1}{3}\left(\frac{\dot{A}}{A}-\frac{\dot{B}}{B}\right)^2$, which leads to a functional relation between the metric potentials of the form $A=B^k$, where $k\neq 1$ is an arbitrary constant. Thorne (1967) extensively discussed the utility of this condition in simplifying anisotropic geometries. Observational analyses further indicate that the present Universe exhibits isotropic Hubble expansion to within approximately $\pm 30\%$ (Kristian and Sachs 1966; Kantowski and Sachs 1966), while redshift observations constrain the ratio $\sigma/H$ to satisfy $\sigma/H\leq 0.3$. Collins et al. (1980) demonstrated that a constant ratio $\sigma/H$ naturally arises in spatially homogeneous cosmologies, justifying the use of the above relation. Another commonly adopted relation in scalar–tensor cosmology is the power-law dependence of the BD scalar field on the average scale factor, expressed as $\phi\propto[a(t)]^n$, where $n$ is a real exponent (Johri and Sudharsan 1989; Johri and Desikan 1994). Various studies (Santhi et al. 2016; Aditya et al. 2020; Aditya et al. 2019; Santhi et al. 2018; Naidu et al. 2021; Bhaskara Rao et al. 2021; Raju et al. 2020a, 2020b) have explored the physical implications of such a dependence. Motivated by these works, and in order to reduce the complexity of the underlying system, we assume the functional form

$$\phi(t)=\phi_0\,[a(t)]^n,$$

where $\phi_0$ is a constant.

Using the relations $A=B^k$ and $\phi(t)=\phi_0\,[a(t)]^n$ in Eqs. (9) and (10), we obtain

$$\frac{\ddot{B}}{\dot{B}}+\left(\frac{3k+3+kn+2n}{3}\right)\frac{\dot{B}}{B}=\frac{8\pi\,\xi(t)\rho_{de}}{(k-1)\phi}\,\frac{A}{\dot{A}}. \quad (12)$$

The interplay between the DE density and the skewness parameter has been widely examined in recent literature. Akarsu and Kilinc (2010) investigated anisotropic DE models incorporating correlations between $\rho_{de}$ and the

skewness parameters. Similarly, Sharif and Zubair (2010) studied the dynamics of anisotropic DE with analogous assumptions. Guided by these works, we posit the following functional relation between $\xi(t)$ and $\rho_{de}$:

$$\xi(t) = \frac{(k-1)\,\xi_0\,\phi\,\dot{A}}{8\pi\rho_{de}\,A}, \tag{13}$$

where $\xi_0$ is a proportionality constant. Comparable choices have been discussed in Adhav (2011); Aditya et al. (2021); Aditya et al. (2022); Prasanthi and Aditya (2021). Substituting Eq. (13) into Eq. (12), the metric potentials are obtained as

$$A = \left(c_1 e^{\xi_0 t} + c_2\right)^{\frac{k\eta_2}{c_2}}, \qquad B = \left(c_1 e^{\xi_0 t} + c_2\right)^{\frac{\eta_2}{c_2}}, \tag{14}$$

where $c_1 = \frac{(k+2)(n+3)}{3}\frac{\eta_1}{\xi_0}$, $c_2 = \frac{(k+2)\eta_2(n+3)}{3}$, and $\eta_1$, $\eta_2$ are integration constants. Using the metric potentials (14), the space-time metric takes the form

$$ds^2 = dt^2 - \left(c_1 e^{\xi_0 t} + c_2\right)^{\frac{2k\eta_2}{c_2}} dx^2 - \left(c_1 e^{\xi_0 t} + c_2\right)^{\frac{2\eta_2}{c_2}} (dy^2 + dz^2). \tag{15}$$

The BD scalar field corresponding to the above geometry is

$$\phi = \phi_0 \left(c_1 e^{\xi_0 t} + c_2\right)^{\frac{n}{n+3}}. \tag{16}$$

The Hubble parameter $H(z)$ is then obtained as

$$\begin{aligned} H &= \frac{1}{3}\left(\frac{\dot{A}}{A} + 2\frac{\dot{B}}{B}\right) = \frac{c_1 e^{\xi_0 t}\,\xi_0}{(n+3)\,(c_1 e^{\xi_0 t} + c_2)} \\ &= \frac{\xi_0}{n+3}\left[1 - c_2(1+z)^{n+3}\right] = \frac{H_0}{1-c_2}\left[1 - c_2(1+z)^{n+3}\right], \end{aligned} \tag{17}$$

where $1 + z = 1/a(t)$, and $\frac{H_0}{1-c_2} = \frac{\xi_0}{n+3}$. In the observational analysis of section III, we constrain the parameters $H_0$, $n$, and $c_2$. Once these are determined, the remaining quantities can be reconstructed from $\xi_0 = \frac{H_0(n+3)}{1-c_2}$, $k = \frac{3c_2}{(n+3)\eta_2} - 2$, for suitably chosen integration constant $\eta_2$ and observationally inferred values of $H_0$, $n$, and $c_2$.

**KHDE:** A generalized single-parameter entropy, known as the Kaniadakis entropy ($\mathcal{K}$-entropy) (Kaniadakis 2001, 2002; Moradpour et al. 2020), is defined as

$$S_{\mathcal{K}} = -\sum_{i=1}^{W} \frac{P_i^{1+\mathcal{K}} - P_i^{1-\mathcal{K}}}{2\mathcal{K}} = \frac{1}{2}\left[\frac{\sum_{i=1}^{W}(P_i^{1-\mathcal{K}} - P_i)}{\mathcal{K}} + \frac{\sum_{i=1}^{W}(P_i^{1+\mathcal{K}} - P_i)}{-\mathcal{K}}\right], \tag{18}$$

where $P_i$ denotes the probability of occupation of the $i^{\text{th}}$ microstate of a classical system. The parameter $\mathcal{K}$ encodes deviations from extensivity, and in the limit $\mathcal{K} \to 0$, the standard Boltzmann–Gibbs entropy is recovered (Kaniadakis 2001, 2002). For an equiprobable distribution $P_i = 1/W$, Eq. (18) yields (Kaniadakis 2001, 2002; Moradpour et al. 2020)

$$S_{\mathcal{K}} = \frac{W^{\mathcal{K}} - W^{-\mathcal{K}}}{2\mathcal{K}} \quad \Longrightarrow \quad S_{\mathcal{K}} = \frac{1}{\mathcal{K}} \sinh(\mathcal{K} S_{\text{BH}}), \tag{19}$$

where $S_{\text{BH}} \propto \dfrac{\mathcal{A}}{4G} = \dfrac{\pi L^2}{G}$ is the Bekenstein–Hawking entropy and $G$ denotes Newton's constant.

Recently, Nojiri et al. (2022b, 2024) introduced a generalized four-parameter entropy function capable of reproducing several important entropy formalisms – such as Tsallis, Rényi, Barrow, Sharma-Mittal, Kaniadakis, and loop quantum gravity entropies – as special limiting cases. The proposed generalized entropy $S_g$ is given by

$$S_g[\alpha_+, \alpha_-, \beta, \gamma] = \frac{1}{\gamma} \left[ \left( 1 + \frac{\alpha_+}{\beta} S_{\text{BH}} \right)^{\beta} - \left( 1 + \frac{\alpha_-}{\beta} S_{\text{BH}} \right)^{-\beta} \right], \tag{20}$$

where $\alpha_+, \alpha_-, \beta$, and $\gamma$ are positive parameters. For the particular limit $\beta \to \infty$ and $\alpha_+ = \alpha_- = \gamma/2 = \mathcal{K}$, Eq. (20) reduces to

$$S_{\mathcal{K}} = \frac{1}{\mathcal{K}} \sinh(\mathcal{K} S_{\text{BH}}), \tag{21}$$

which matches the Kaniadakis entropy in Eq. (19). Using the holographic principle, the energy density associated with the Kaniadakis entropy (19) takes the form

$$\rho_{de} \propto \frac{S_{\mathcal{K}}}{L^4} \quad \Longrightarrow \quad \rho_{de} = \frac{3c^2 M_p^2}{\mathcal{K} L^4} \sinh\left( \frac{\mathcal{K} \pi L^2}{G} \right), \tag{22}$$

where $M_p^2 = 1/(8\pi G)$ is the reduced Planck mass, $L$ is the IR cutoff length scale, $c$ is a model constant, and $\mathcal{K}$ is the Kaniadakis parameter. In the Brans–Dicke (BD) framework, the gravitational coupling is dynamical, with $G = 1/\phi$. Substituting this relation into Eq. (22), the KHDE density becomes

$$\rho_{de} = \frac{3c^2 \phi}{8\pi \mathcal{K} L^4} \sinh\left( \mathcal{K} \pi L^2 \phi \right). \tag{23}$$

In HDE models, the choice of the IR cutoff plays a decisive role in determining cosmic evolution. The Hubble horizon, $L = H^{-1}$, is one of the most natural and physically motivated options. An alternative is the GO cutoff,

$$L = \left( \alpha_1 H^2 + \alpha_2 \dot{H} \right)^{-1/2},$$

where $\alpha_1$ and $\alpha_2$ are dimensionless constants. Motivated by these considerations, we construct two dynamical KHDE models by adopting these two IR cutoffs.

**Model-1: KHDE model with Hubble horizon** The Hubble radius $H^{-1}$ represents one of the most fundamental cosmological length scales, as it is directly linked to the expansion rate of the universe. Employing it as the IR cutoff therefore provides a natural and physically motivated bridge between DE and the cosmic expansion history. Within the KHDE framework, the energy density is modified through the Kaniadakis entropy formalism, and adopting $L = H^{-1}$ leads to a dynamically evolving DE component whose behaviour tracks the evolution of the Hubble parameter. This feature allows the model to naturally accommodate the transition from a decelerated expansion phase to the current accelerated epoch. Consequently, the Hubble horizon cutoff enables the KHDE model to describe both the matter-dominated era and the late-time acceleration in a unified manner.

By taking the Hubble horizon as the IR cutoff (i.e., $L = H^{-1}$), the KHDE energy density becomes

$$\rho_{de} = \frac{3c^2H^4\phi}{8\pi\mathcal{K}}\sinh\left(\frac{\mathcal{K}\pi\phi}{H^2}\right), \tag{24}$$

where $c^2$ is an undetermined model parameter, $\mathcal{K}$ belongs to the real domain, and $H = \dot{a}/a$ denotes the Hubble parameter.

Using Eqs. (14), (16) and (17) in Eq. (24), the KHDE energy density for model-1 becomes

$$\rho_{de} = \frac{3}{8}\frac{c^2c_1^4\,(e^{\xi_0 t})^4\,\xi_0^4\,\phi_0}{(n+3)^4\left(c_1e^{\xi_0 t}+c_2\right)^4\pi\,\mathcal{K}}\left(c_1e^{\xi_0 t}+c_2\right)^{\frac{n}{n+3}} \times \sinh\left[\frac{\pi\,\mathcal{K}\,\phi_0(n+3)^2\left(c_1e^{\xi_0 t}+c_2\right)^2}{c_1^2(e^{\xi_0 t})^2\,\xi_0^2}\left(c_1e^{\xi_0 t}+c_2\right)^{\frac{n}{n+3}}\right]. \tag{25}$$

The BT-$I$ universe with KHDE inside the framework of BDR theory of gravity is shown by Eq. (15), the scalar field (16), and the energy density (25). Using Eqs. (14)-(16) in the field Eqs. (8)–(11) and (25), we get the EoS parameter as

$$\begin{aligned}\omega_{de} = \frac{8}{3}\frac{(n+3)^4\,(c_1e^{\xi_0 t}+c_2)^4\,\pi\,\mathcal{K}}{c^2\,c_1^4\,(e^{\xi_0 t})^4\,\xi_0^4\,\phi_0}\Bigg[\frac{\lambda-1}{2-4\lambda}\Bigg(\frac{1}{8}\frac{\phi_0}{\pi}(c_1e^{\xi_0 t}+c_2)^{\frac{n}{n+3}}\Big(\frac{2k\eta_2^2c_1^2\xi_0^2(e^{\xi_0 t})^2}{c_2^2(c_1e^{\xi_0 t}+c_2)^2}\\ + \frac{\eta_2^2c_1^2\xi_0^2(e^{\xi_0 t})^2}{c_2^2(c_1e^{\xi_0 t}+c_2)^2} - \frac{wn^2c_1^2\xi_0^2(e^{\xi_0 t})^2(2-3\lambda)}{(n+3)^2(c_1e^{\xi_0 t}+c_2)^2(2-4\lambda)}\Big)\\ - \frac{(1+\lambda)k\eta_2c_1^2\xi_0^2(e^{\xi_0 t})^2n}{(2-4\lambda)c_2(c_1e^{\xi_0 t}+c_2)^2(n+3)} - \frac{(1+\lambda)\eta_2c_1^2\xi_0^2(e^{\xi_0 t})^2n}{(1-2\lambda)c_2(c_1e^{\xi_0 t}+c_2)^2(n+3)}\\ - \frac{(3-3\lambda)\Big(n^2c_1^2\xi_0^2(e^{\xi_0 t})^2+n(n+3)c_1c_2\xi_0^2e^{\xi_0 t}\Big)}{(n+3)^2(c_1e^{\xi_0 t}+c_2)^2(2-4\lambda)}\Bigg)\Bigg]\end{aligned}$$

$$-\frac{1}{8}\frac{(1-\lambda)c_1e^{\xi_0 t}\xi_0^2(k-1)\eta_2\phi_0}{(c_1e^{\xi_0 t}+c_2)c_2\pi(2-4\lambda)}(c_1e^{\xi_0 t}+c_2)^{\frac{n}{n+3}}\Bigg]$$

$$-\frac{1-3\lambda}{2-4\lambda}\Bigg[\frac{1}{8}\frac{\phi_0}{\pi}(c_1e^{\xi_0 t}+c_2)^{\frac{n}{n+3}}\Big(\frac{2\eta_2^2c_1^2\xi_0^2(e^{\xi_0 t})^2+\eta_2c_1c_2^2\xi_0^2(e^{\xi_0 t})}{c_2^2(c_1e^{\xi_0 t}+c_2)^2}$$

$$+\frac{\eta_2^2c_1^2\xi_0^2(e^{\xi_0 t})^2}{c_2^2(c_1e^{\xi_0 t}+c_2)^2}-\frac{wn^2c_1^2\xi_0^2(e^{\xi_0 t})^2\lambda}{(n+3)^2(c_1e^{\xi_0 t}+c_2)^2(2-4\lambda)}\Big)$$

$$-\frac{(3-3\lambda)k\eta_2c_1^2\xi_0^2(e^{\xi_0 t})^2n}{(2-4\lambda)c_2(c_1e^{\xi_0 t}+c_2)^2(n+3)}-\frac{(1+\lambda)\eta_2c_1^2\xi_0^2(e^{\xi_0 t})^2n}{(1-2\lambda)c_2(c_1e^{\xi_0 t}+c_2)^2(n+3)}$$

$$-\frac{(1+\lambda)\Big(n^2c_1^2\xi_0^2(e^{\xi_0 t})^2+n(n+3)c_1c_2\xi_0^2e^{\xi_0 t}\Big)}{(n+3)^2(c_1e^{\xi_0 t}+c_2)^2(2-4\lambda)}$$

$$-\frac{1}{8}\frac{(3\lambda-1)c_1e^{\xi_0 t}\xi_0^2(k-1)\eta_2\phi_0}{(c_1e^{\xi_0 t}+c_2)c_2\pi(2-4\lambda)}(c_1e^{\xi_0 t}+c_2)^{\frac{n}{n+3}}\Bigg]$$

$$\times\left(-\frac{(1-3\lambda)(1+\lambda)}{(2-4\lambda)^2}+\frac{(3-3\lambda)(\lambda-1)}{(2-4\lambda)^2}\right)^{-1}(c_1e^{\xi_0 t}+c_2)^{-\frac{n}{n+3}}$$

$$\times\left[\sinh\left(\frac{\pi\mathcal{K}\phi_0(n+3)^2(c_1e^{\xi_0 t}+c_2)^2}{c_1^2(e^{\xi_0 t})^2\xi_0^2}(c_1e^{\xi_0 t}+c_2)^{\frac{n}{n+3}}\right)\right]^{-1} \tag{26}$$

and the skewness parameter as

$$\xi(t)=\frac{1}{3}\frac{(n+3)^4\left(c_1e^{\xi_0 t}+c_2\right)^3\mathcal{K}\left(k-1\right)\eta_2}{c^2\,c_1^3\,(e^{\xi_0 t})^3\,\xi_0^2\,c_2}$$

$$\times\left[\sinh\left(\frac{\pi\,\mathcal{K}\,\phi_0\,(n+3)^2\left(c_1e^{\xi_0 t}+c_2\right)^2}{c_1^2(e^{\xi_0 t})^2\,\xi_0^2}\left(c_1e^{\xi_0 t}+c_2\right)^{\frac{n}{n+3}}\right)\right]^{-1}. \tag{27}$$

**Model-2: KHDE model with GO horizon** The GO cutoff is constructed solely from local cosmological quantities, namely the Hubble parameter $H$ and its time derivative $\dot{H}$, unlike non-local choices such as the particle horizon or the future event horizon. Nojiri and Odintsov (2006) proposed a generalized HDE framework in which the IR cutoff is defined as a combination of several fundamental FRW parameters, including the Hubble rate, the particle and future event horizons, the lifetime of a finite-age universe, and even the cosmological constant. This generalized formulation, known as the Nojiri–Odintsov HDE cutoff, has been shown to allow phantom divide crossing and to address the coincidence problem in the presence of matter. The GO cutoff arises naturally as a special case of this broader Nojiri–Odintsov scenario. Since the GO cutoff depends only on local properties of the universe, it avoids causality issues and does not require information about the future evolution of the cosmos. When incorporated within the KHDE framework, the GO cutoff leads to

a richer and more flexible dynamical behavior. The explicit appearance of the $\dot{H}$ term enables the KHDE model to describe both the decelerated expansion associated with matter- or radiation-dominated epochs and the accelerated expansion characteristic of DE, providing a unified picture of cosmic evolution. Moreover, the free parameters $\alpha_1$ and $\alpha_2$ in the GO cutoff offer significant flexibility in shaping the DE equation-of-state parameter $\omega_{de}$. Depending on the chosen parameter space, the model can effectively mimic quintessence-like, cosmological-constant-like, or phantom-like behavior, thereby allowing for better compatibility with observational data.

In this scenario, we use a KHDE model with the GO horizon cutoff $L = (\alpha_1 H^2 + \alpha_2 \dot{H})^{-\frac{1}{2}}$ (Granda and Oliveros 2008, 2009), we get

$$\rho_{de} = \frac{3}{8}\frac{c^2\,\phi_0}{\pi\,\mathcal{K}}\left(c_1 e^{\xi_0 t}+c_2\right)^{\frac{n}{n+3}} \times \sinh\left[\left(\pi\,\mathcal{K}\,\phi_0\left(c_1 e^{\xi_0 t}+c_2\right)^{\frac{n}{n+3}}\right)\right.$$
$$\left.\times\left(\frac{\alpha_1\,c_1^2(e^{\xi_0 t})^2\xi_0^2}{(n+3)^2\left(c_1 e^{\xi_0 t}+c_2\right)^2}+\frac{\alpha_2}{n+3}\left(\frac{c_1\xi_0^2 e^{\xi_0 t}}{\left(c_1 e^{\xi_0 t}+c_2\right)}-\frac{c_1^2(e^{\xi_0 t})^2\xi_0^2}{\left(c_1 e^{\xi_0 t}+c_2\right)^2}\right)\right)^{-1}\right]$$
$$\times\left[\frac{\alpha_1\,c_1^2(e^{\xi_0 t})^2\xi_0^2}{(n+3)^2\left(c_1 e^{\xi_0 t}+c_2\right)^2}+\frac{\alpha_2}{n+3}\left(\frac{c_1\xi_0^2 e^{\xi_0 t}}{\left(c_1 e^{\xi_0 t}+c_2\right)}-\frac{c_1^2(e^{\xi_0 t})^2\xi_0^2}{\left(c_1 e^{\xi_0 t}+c_2\right)^2}\right)\right]^2. \quad (28)$$

The BT-$I$ universe with KHDE inside the framework of BDR theory of gravity is shown by Eq. (15), the scalar field (16), and the energy density (28). Using Eqs. (14)-(16) in the field Eqs. (8)-(11) and (28), we get the EoS parameter as

$$\omega_{de} = \frac{8}{3}\frac{\pi\,\mathcal{K}}{c^2\phi_0}\left[\frac{\lambda-1}{2-4\lambda}\left(\frac{1}{8}\frac{\phi_0}{\pi}\left(c_1 e^{\xi_0 t}+c_2\right)^{\frac{n}{n+3}}\right.\right.$$
$$\times\left\{\frac{2k\eta_2^2c_1^2\xi_0^2(e^{\xi_0 t})^2}{c_2^2\left(c_1 e^{\xi_0 t}+c_2\right)^2}+\frac{\eta_2^2c_1^2\xi_0^2(e^{\xi_0 t})^2}{c_2^2\left(c_1 e^{\xi_0 t}+c_2\right)^2}-\frac{wn^2c_1^2\xi_0^2(e^{\xi_0 t})^2(2-3\lambda)}{(n+3)^2\left(c_1 e^{\xi_0 t}+c_2\right)^2(2-4\lambda)}\right.$$
$$-\frac{(1+\lambda)k\eta_2c_1^2\xi_0^2(e^{\xi_0 t})^2n}{(2-4\lambda)c_2\left(c_1 e^{\xi_0 t}+c_2\right)^2(n+3)}-\frac{(1+\lambda)\eta_2c_1^2\xi_0^2(e^{\xi_0 t})^2n}{(1-2\lambda)c_2\left(c_1 e^{\xi_0 t}+c_2\right)^2(n+3)}$$
$$\left.\left.-\frac{(3-3\lambda)\left(n^2c_1^2\xi_0^2(e^{\xi_0 t})^2+n(n+3)c_1c_2\xi_0^2e^{\xi_0 t}\right)}{(n+3)^2\left(c_1 e^{\xi_0 t}+c_2\right)^2(2-4\lambda)}\right\}\right)$$
$$\left.-\frac{1}{8}\frac{(1-\lambda)c_1e^{\xi_0 t}\xi_0^2(k-1)\eta_2\phi_0}{(c_1e^{\xi_0 t}+c_2)c_2\pi(2-4\lambda)}\left(c_1 e^{\xi_0 t}+c_2\right)^{\frac{n}{n+3}}\right]$$
$$-\frac{1-3\lambda}{2-4\lambda}\left[\frac{1}{8}\frac{\phi_0}{\pi}\left(c_1 e^{\xi_0 t}+c_2\right)^{\frac{n}{n+3}}\left(\frac{2\eta_2^2c_1^2\xi_0^2(e^{\xi_0 t})^2+\eta_2c_1c_2^2\xi_0^2e^{\xi_0 t}}{c_2^2(c_1e^{\xi_0 t}+c_2)^2}\right.\right.$$

$$+\frac{\eta_2^2 c_1^2 \xi_0^2 (e^{\xi_0 t})^2}{c_2^2 (c_1 e^{\xi_0 t}+c_2)^2} - \frac{w n^2 c_1^2 \xi_0^2 (e^{\xi_0 t})^2 \lambda}{(n+3)^2 (c_1 e^{\xi_0 t}+c_2)^2 (2-4\lambda)}\Bigg)$$
$$-\frac{(3-3\lambda) k \eta_2 c_1^2 \xi_0^2 (e^{\xi_0 t})^2 n}{(2-4\lambda) c_2 (c_1 e^{\xi_0 t}+c_2)^2 (n+3)} - \frac{(1+\lambda)\eta_2 c_1^2 \xi_0^2 (e^{\xi_0 t})^2 n}{(1-2\lambda) c_2 (c_1 e^{\xi_0 t}+c_2)^2 (n+3)}$$
$$-\frac{(1+\lambda)\big(n^2 c_1^2 \xi_0^2 (e^{\xi_0 t})^2 + n(n+3) c_1 c_2 \xi_0^2 e^{\xi_0 t}\big)}{(n+3)^2 (c_1 e^{\xi_0 t}+c_2)^2 (2-4\lambda)}$$

$$-\frac{1}{8}\frac{(3\lambda-1) c_1 e^{\xi_0 t} \xi_0^2 (k-1)\eta_2 \phi_0}{(c_1 e^{\xi_0 t}+c_2) c_2 \pi (2-4\lambda)} \big(c_1 e^{\xi_0 t}+c_2\big)^{\frac{n}{n+3}}\Bigg]$$

$$\times \left[-\frac{(1-3\lambda)(1+\lambda)}{(2-4\lambda)^2} + \frac{(3-3\lambda)(\lambda-1)}{(2-4\lambda)^2}\right]^{-1} \big(c_1 e^{\xi_0 t}+c_2\big)^{-\frac{n}{n+3}}$$

$$\times \left[\frac{\alpha_1 c_1^2 (e^{\xi_0 t})^2 \xi_0^2}{(n+3)^2 (c_1 e^{\xi_0 t}+c_2)^2} + \alpha_2 \left(\frac{c_1 \xi_0^2 e^{\xi_0 t}}{(n+3)(c_1 e^{\xi_0 t}+c_2)} - \frac{c_1^2 (e^{\xi_0 t})^2 \xi_0^2}{(n+3)(c_1 e^{\xi_0 t}+c_2)^2}\right)\right]^{-2}$$

$$\times \Bigg\{ \sinh\Bigg\{ \pi \mathcal{K} \phi_0 \left(c_1 e^{\xi_0 t}+c_2\right)^{\frac{n}{n+3}} \Bigg\{ \frac{\alpha_1 c_1^2 (e^{\xi_0 t})^2 \xi_0^2}{(n+3)^2 (c_1 e^{\xi_0 t}+c_2)^2}$$
$$+\alpha_2 \left(\frac{c_1 \xi_0^2 e^{\xi_0 t}}{(n+3)(c_1 e^{\xi_0 t}+c_2)} - \frac{c_1^2 (e^{\xi_0 t})^2 \xi_0^2}{(n+3)(c_1 e^{\xi_0 t}+c_2)^2}\right) \Bigg\}^{-1} \Bigg\} \Bigg\}^{-1}, \tag{29}$$

and we find the skewness parameter as

$$\xi = \frac{1}{3}\frac{\mathcal{K}(k-1)\xi_0^2 \eta_2 c_1 e^{\xi_0 t}}{c^2 c_2 \big(c_1 e^{\xi_0 t}+c_2\big)} \Bigg\{ \frac{\alpha_1 c_1^2 (e^{\xi_0 t})^2 \xi_0^2}{(n+3)^2 \big(c_1 e^{\xi_0 t}+c_2\big)^2}$$
$$+\alpha_2 \left(\frac{c_1 \xi_0^2 e^{\xi_0 t}}{(n+3)\big(c_1 e^{\xi_0 t}+c_2\big)} - \frac{c_1^2 (e^{\xi_0 t})^2 \xi_0^2}{(n+3)\big(c_1 e^{\xi_0 t}+c_2\big)^2}\right) \Bigg\}^{-2}$$
$$\times \Bigg\{ \sinh\Bigg\{ \pi \mathcal{K} \phi_0 \left(c_1 e^{\xi_0 t}+c_2\right)^{\frac{n}{n+3}} \Bigg\{ \frac{\alpha_1 c_1^2 (e^{\xi_0 t})^2 \xi_0^2}{(n+3)^2 \big(c_1 e^{\xi_0 t}+c_2\big)^2}$$
$$+\alpha_2 \left(\frac{c_1 \xi_0^2 e^{\xi_0 t}}{(n+3)\big(c_1 e^{\xi_0 t}+c_2\big)} - \frac{c_1^2 (e^{\xi_0 t})^2 \xi_0^2}{(n+3)\big(c_1 e^{\xi_0 t}+c_2\big)^2}\right) \Bigg\}^{-1} \Bigg\} \Bigg\}^{-1}. \tag{30}$$

## 3 Model parameters estimation using observational data

To constrain the free parameters of the proposed cosmological model, we make use of the MCMC sampling technique, which enables a systematic statistical comparison between the theoretical predictions and contemporary observational datasets. In this analysis, we incorporate measurements of the Hubble parameter $H(z)$ as well as BAO. The MCMC approach has become a standard and powerful tool in modern cosmology, particularly for multi-parameter

models, as it efficiently explores high-dimensional likelihood surfaces and yields reliable posterior probability distributions. Within a Bayesian framework, this method offers a consistent and unbiased procedure for confronting theoretical cosmologies with empirical data. In the present study, MCMC analysis is carried out to evaluate the observational compatibility of the model parameters and to determine whether the resulting cosmic expansion history is consistent with current observations.

### 3.1 Cosmic chronometer dataset

To examine the redshift evolution of the Hubble parameter, we employ the CC method, which estimates $H(z)$ from differential age measurements of passively evolving galaxies. The strength of this technique lies in its independence from specific cosmological assumptions or early-Universe physics, making it an exceptionally robust probe of late-time cosmic dynamics. In this work, we use a compilation of 31 CC data points spanning the redshift range $0.07 \leq z \leq 2.41$, as reported in Moresco (2015) and Moresco et al. (2012, 2016). The observed and theoretical values of the Hubble parameter are denoted by $H_{\rm obs}(z_i)$ and $H_{\rm th}(z_i)$, respectively, with $\sigma(z_i)$ representing the corresponding measurement uncertainties. The chi-squared statistic used to quantify the goodness of fit is

$$\chi^2_{\rm CC} = \sum_{i=1}^{31} \frac{[H_{\rm th}(z_i) - H_{\rm obs}(z_i)]^2}{\sigma^2(z_i)}. \tag{31}$$

This expression provides a direct measure of how effectively the theoretical model reproduces the observed evolution of the Hubble parameter across the sampled redshift range.

### 3.2 BAO Dataset

Baryon Acoustic Oscillation (BAO) measurements serve as another key observational probe, offering independent constraints on the expansion history of the Universe. BAO signatures originate from acoustic waves propagating in the tightly coupled photon–baryon plasma prior to recombination, imprinting a characteristic scale in the matter distribution. This scale acts as a standard ruler, enabling precise distance measurements and constraints on the expansion rate at various cosmic epochs. In this analysis, we utilize 26 line-of-sight BAO data points from Mishra (2024) and Rana et al. (2025). The observational and theoretical Hubble parameter values are denoted by $H_{\rm obs}(z_i)$ and $H_{\rm th}(z_i)$, with $\sigma_H(z_i)$ denoting the measurement uncertainties. The chi-squared statistic for the BAO dataset is given by

$$\chi^2_{\rm BAO} = \sum_{i=1}^{26} \frac{[H_{\rm th}(z_i) - H_{\rm obs}(z_i)]^2}{\sigma^2_H(z_i)}. \tag{32}$$

The theoretical $H(z)$ values are calculated using the cosmographic expansion of the model, following a procedure analogous to that employed in the CC

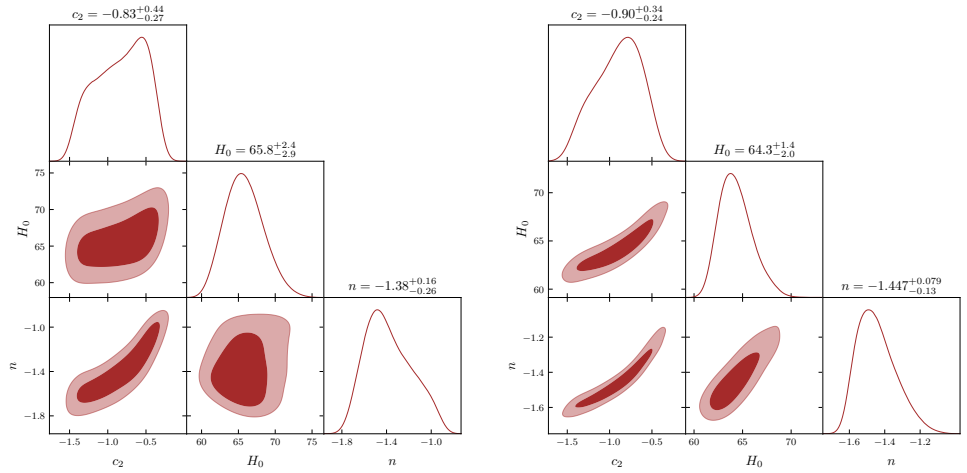


(a) CC Dataset (b) CC+BAO Dataset

**Fig. 1.** The 2D contour plots of $H_0, n, c_2$ at $\sigma 1$ and $\sigma 2$ level of confidence in the joint MCMC analysis of CC and CC+BAO datasets.

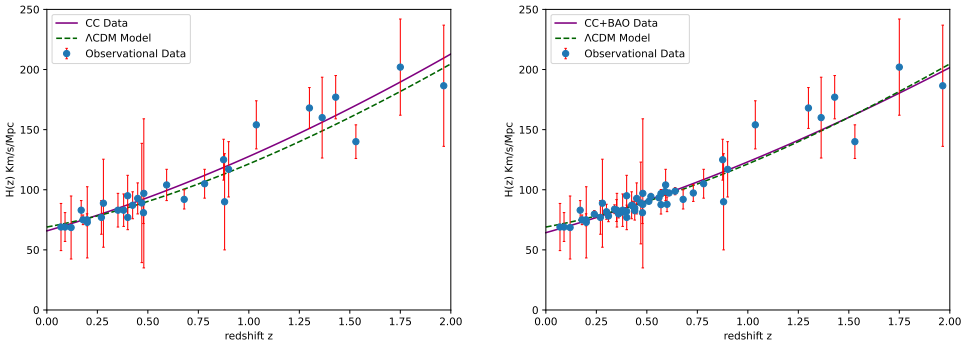


(a) CC Dataset (b) CC+BAO Dataset

**Fig. 2.** Evolution of Hubble parameter $H(z)$ versus redshift $z$. The solid line represents our model and dotted-line indicates the $\Lambda$CDM model with $\Omega_{m0} = 0.3$ and $\Omega_{de0} = 0.7$. The dots are shown the observational dataset with error bar.

analysis. The inclusion of BAO data provides a complementary test to the CC measurements, helping to break parameter degeneracies and significantly enhancing the statistical robustness of the derived cosmological constraints.

Using the datasets mentioned above, we have found the best-fit values for the parameters $n$, $H_0$, and $c_2$. The best-fit values and estimated values are determined and presented in Table 1.

The two-dimensional contour plots presented in Fig. 1 illustrate the joint posterior distributions of the cosmological parameters $H_0$, $n$, and $c_2$ obtained from MCMC analysis using CC data and a combined CC+BAO dataset. The shaded regions correspond to the $1\sigma$ and $2\sigma$ confidence levels, allowing us to

**Table 1.** MCMC constraints on the model parameters for the CC and CC+BAO datasets, including derived parameters $\xi_0$ and $k$ with propagated uncertainties.

| **Parameter** | **Prior** | **Datasets** | |
|---|---|---|---|
| | | **CC** | **CC + BAO** |
| $H_0$ | (60, 80) | $65.8^{+2.4}_{-2.9}$ | $64.3^{+1.4}_{-2.0}$ |
| $c_2$ | $(-2, 0)$ | $-0.83^{+0.44}_{-0.27}$ | $-0.90^{+0.34}_{-0.24}$ |
| $n$ | $(-2, -1)$ | $-1.38^{+0.16}_{-0.26}$ | $-1.447^{+0.079}_{-0.13}$ |
| $\xi_0 = \dfrac{H_0(n+3)}{1-c_2}$ | – | $58.25 \pm 13.79$ | $52.56 \pm 8.88$ |
| $\eta_1$ | – | $+0.40$ | $+0.40$ |
| $\eta_2$ | – | $-0.52$ | $-0.59$ |
| $k = \dfrac{3c_2}{(n+3)\eta_2} - 2$ | – | 0.956 | 0.947 |

examine both the preferred parameter space and the correlations among the parameters within the chosen cosmological model. For the CC dataset alone (Fig. 1(a)), the reconstructed posterior distributions show moderately broad contours, which reflects the intrinsic limitations of CC measurements.

Figure 2 displays the reconstructed Hubble parameter $H(z)$ as a function of redshift for two dataset combinations: (a) CC alone and (b) CC combined with BAO (CC+BAO). The solid curve corresponds to the best–fit prediction of the model under consideration, while the dashed curve shows the fiducial $\Lambda$CDM behaviour with $\Omega_{m0} = 0.3$ and $\Omega_{de0} = 0.7$. The blue points with vertical error bars are the observational $H(z)$ measurements used in the joint MCMC analysis. Both panels show that our models follow the overall trend of the observational $H(z)$ data across the redshift range $0 \lesssim z \lesssim 2$. At low redshift ($z \lesssim 0.5$) the model curve and the $\Lambda$CDM curve are nearly coincident and lie well within the observational uncertainties. This behaviour indicates that the late-time expansion history predicted by the model is consistent with established late-time probes. At higher redshifts ($z \gtrsim 1.2$) the observational uncertainties are larger and the model prediction remains consistent with the data while showing a mild departure from the $\Lambda$CDM dashed line in some realizations.

In summary, the $H(z)$ plots show that the proposed model reproduces the observed expansion history within current uncertainties and produces only modest departures from $\Lambda$CDM. The addition of BAO tightens constraints and slightly favors a lower global $H_0$; however, demonstrating a clear detection of new physics beyond $\Lambda$CDM will require more precise high–redshift measurements and a full model comparison using statistical information criteria.

## 4 Cosmological parameters

In this section, we analyze the expansion behavior of the universe for the constructed KHDE models (Model-1 and Model-2) using well-established cosmological diagnostics, including the EoS parameter $\omega_{de}$, the squared sound speed

$v_s^2$, the deceleration parameter $q$, the Om-diagnostic $Om(z)$, thermodynamics and cosmic coincidence. Additionally, we employ cosmological diagnostic planes such as $\omega_{de} - \omega'_{de}$, the statefinder pair $(r, s)$, and the $r - q$ plane. Here, we have used the parameter values as shown in table 1 and $c = \phi_0 = 1.87$, $w = 0.4$, $\alpha_1 = 0.98$, $\alpha_2 = 0.01$, $\lambda = 0.6$ for graphical representation of the models.

## Scalar field

Fig. 3 (see Appendix[1]) depicts the evolution of the scalar field $\phi(z)$ as a function of redshift $z$ for the CC dataset and the combined CC+BAO dataset. The shaded regions represent the $1\sigma$ confidence intervals of the parameter $n$ obtained from the MCMC analysis. In both cases, the scalar field exhibits a monotonic increase with redshift, indicating that it had a larger magnitude in the past and gradually decreases toward the present epoch. This behaviour is typical of scalar–tensor and Brans–Dicke–type cosmological models, where the scalar field governs the effective gravitational coupling or contributes to cosmic acceleration. At higher redshifts ($z \gtrsim 1$), the rapid growth of $\phi(z)$ reflects matter domination, during which the scalar field dynamics are strongly influenced by the background expansion. In contrast, at lower redshifts ($z \lesssim 0.5$), the evolution becomes slower as dark energy starts to dominate. The CC-only results show broader confidence regions, while the inclusion of BAO data significantly tightens the constraints, leading to a more precise reconstruction of $\phi(z)$.

## Deceleration parameter

Fig. 4 (see Appendix) illustrates the evolution of the deceleration parameter $q(z)$ as a function of redshift for both the CC dataset and the combined CC+BAO dataset. The shaded region in each panel represents the $1\sigma$ confidence interval of $n$ reconstructed from the MCMC-derived cosmological parameters. The deceleration parameter provides a direct diagnostic of the expansion history of the Universe, since its sign determines whether cosmic expansion is accelerating or decelerating. Specifically, a positive value ($q > 0$) corresponds to decelerated expansion, $q = 0$ represents a transition point, and a negative value ($-1 \leq q < 0$) corresponds to accelerated expansion. A limiting value $q = -1$ indicates de Sitter exponential expansion, while $q < -1$ corresponds to super-accelerated or phantom-like behaviour. The parameter for our model is defined by the relation

$$q = -1 - \frac{\dot{H}}{H^2} = -1 - \frac{c_2\,(n+3)}{c_1 \mathrm{e}^{\xi_0 t}},$$

where $H$ is the Hubble parameter.

Fig. 4 (see Appendix) clearly shows a transition from an early decelerating phase to a late-time accelerating phase. At high redshift, typically $z \gtrsim 1$,

[1] The Appendix is available only in electronic form on the site of the Bulgarian Astronomical Journal, vol.45

the curves lie in the region $q > 0$, indicating that the Universe was experiencing decelerated expansion. This behaviour is consistent with expectations from standard cosmology, in which the matter-dominated era is characterised by gravitational attraction that slows down the expansion. As the redshift decreases towards the present epoch, the deceleration parameter gradually decreases and eventually becomes negative. The moment at which $q(z)$ crosses zero marks the transition from deceleration to acceleration. From the reconstructed curves, this transition occurs around $z_t \approx 0.6 - 0.8$ for CC data, $z_t \approx 0.5 - 0.7$ for CC+BAO data. These values agree well with current observational estimates from Type Ia supernovae, BAO, and other late-time probes, which typically place the transition redshift in the range $z_t \sim 0.5 - 1.0$. The alignment of our results with these independent observations supports the consistency and viability of the model.

The smooth transition of $q(z)$ from positive to negative values suggests that the model naturally incorporates a mechanism capable of driving late-time acceleration. The inclusion of BAO data results in a more precise determination of both the transition redshift and the present deceleration value. This reflects the well-known ability of BAO to break degeneracies among parameters that directly influence the slope of $H(z)$ and therefore the behaviour of $q(z)$. These findings support the ability of the considered model to reproduce the essential features of the observed cosmic acceleration.

**Statefinder diagnostic**

Fig. 5 (see Appendix) displays the evolutionary trajectories of the models in the statefinder plane, characterized by the pair of geometrical diagnostics $(r, s)$ introduced by Sahni et al. (2003). The statefinder parameters are constructed from higher-order derivatives of the scale factor and are given by

$$r = \frac{\dddot{a}}{aH^3} = 1 + 3\,\frac{c_2\,(n+3)}{c_1 \mathrm{e}^{\xi_0 t}} + \frac{{c_2}^2\,(n+3)^2}{{c_1}^2\,(\mathrm{e}^{\xi_0 t})^2} - \frac{c_2\,(n+3)^2}{c_1 \mathrm{e}^{\xi_0 t}},$$

$$s = \frac{r-1}{3\left(q-\frac{1}{2}\right)} = \left(3\,\frac{c_2\,(n+3)}{c_1 \mathrm{e}^{\xi_0 t}} + \frac{{c_2}^2\,(n+3)^2}{{c_1}^2\,(\mathrm{e}^{\xi_0 t})^2} - \frac{c_2\,(n+3)^2}{c_1 \mathrm{e}^{\xi_0 t}}\right) \times \left(-4.5 - 3\,\frac{c_2\,(n+3)}{c_1 \mathrm{e}^{\xi_0 t}}\right)^{-1}. \tag{33}$$

Unlike the Hubble parameter $H$ and the deceleration parameter $q$, which measure the expansion rate and its first derivative, respectively, the statefinder pair probes the third derivative of the scale factor. This higher-order sensitivity enables the statefinder diagnostic to effectively distinguish between competing DE models that may share identical present-day values of $H$ and $q$. Thus, the $(r, s)$ plane serves as a powerful tool to identify the dynamical nature of DE and to determine the deviation of any proposed model from the standard $\Lambda$CDM cosmology. The most important benchmarks in the statefinder plane include:

– $(r, s) = (1, 1)$ corresponds to the cold dark matter (CDM) universe with no DE component.

- $(r, s) = (1, 0)$ represents the fixed point of the $\Lambda$CDM model.
- Regions with $r < 1$ and $s > 0$ typically characterize quintessence or phantom-like DE models.

These fixed points allow us to compare the predictions of our model with standard cosmologies and classify its evolutionary path.

The left panel of Fig. 5 (see Appendix) shows the trajectory obtained from the CC dataset alone, while the right panel corresponds to the combined CC+BAO dataset. In both panels, the model exhibits a characteristic loop-like trajectory in the $(r, s)$ plane. The arrows indicate the direction of evolution from the past (high redshift) toward the present and future epochs. At early times (higher redshift), the model begins in a region with $r < 1$ and $s > 0$, which corresponds to a quintessence or phantom-like behaviour. This indicates that the model initially behaves like a non-$\Lambda$ DE scenario, with the DE component contributing dynamically to the expansion rate. As the Universe evolves, the trajectories gradually move toward the $\Lambda$CDM fixed point $(r, s) = (1, 0)$. The proximity of the present-day trajectory to the $\Lambda$CDM point indicates that the model closely mimics the behaviour of the cosmological constant at late times. The most notable difference between the CC-only and CC+BAO trajectories is the degree of tightening in the reconstructed region. With BAO data included, the loop becomes narrower and the trajectory approaches the $\Lambda$CDM point more closely, showing that the joint dataset places stronger constraints on the DE evolution. This suggests that the model behaves increasingly like $\Lambda$CDM at low redshift when BAO information is incorporated. In summary, the statefinder diagnostic reveals that the proposed cosmological model interpolates between a dynamical DE regime at early times and a $\Lambda$CDM-like behaviour at late times. The addition of BAO data significantly tightens the constraints and strengthens the compatibility of the model with the standard cosmological scenario, while still allowing for mild departures characteristic of dynamical DE models.

### Evolution of models in the $r - q$ plane

Fig. 6 (see Appendix) depicts the evolutionary behaviour of the models in the $r$–$q$ plane for both the CC dataset and the combined CC+BAO dataset. The pair $(r, q)$ consists of the statefinder parameter $r$, involving the third derivative of the scale factor, and the deceleration parameter $q$, involving the second derivative. Because these parameters encode higher-order geometrical information, the $r$–$q$ diagram provides an effective tool to distinguish between various cosmological models that may appear degenerate when interpreted only through $H(z)$ or $q(z)$ alone.

Two important fixed points are marked in the figure:

- $(r, q) = (1, 0.5)$ corresponds to the Standard Cold Dark Matter (SCDM) model. This point represents a purely matter-dominated universe with no cosmological constant or DE component, where the expansion is decelerating.
- $(r, q) = (1, -1)$ represents the Steady-State (SS) or de Sitter model, characterized by constant exponential expansion (i.e. $q = -1$). This fixed point corresponds to a cosmological constant dominated universe.

The standard $\Lambda$CDM model evolves monotonically along the vertical line $r = 1$, moving from the SCDM point $(1, 0.5)$ at early times to the SS point $(1, -1)$ at late times. The dotted red line in the figure illustrates this behaviour. The trajectories derived from the CC and CC+BAO datasets show a characteristic curvature in the $(r, q)$ plane, different from the strictly vertical evolution of $\Lambda$CDM. Instead of evolving solely along $r = 1$, the trajectories initially deviate into the region with $r < 1$ and later curve back toward the de Sitter point. At high redshift (early cosmic times), the curves lie closer to the region $q > 0$, consistent with the expected decelerated expansion during matter domination. As the universe evolves, the trajectories bend downward (toward lower $q$ values) and also move rightward (toward higher $r$). This behaviour reflects the transition from deceleration to acceleration, driven by the emergence of the effective DE component. Eventually, the curves approach the point $(r, q) = (1, -1)$, indicating that the model tends asymptotically toward a de Sitter-like accelerated expansion. In summary, the $r$–$q$ analysis reveals that the model exhibits dynamical DE behaviour at early times, transitions smoothly through the observationally favoured acceleration epoch, and ultimately approaches a de Sitter Universe. The improved constraints with CC+BAO further strengthen the evidence for this behaviour and highlight the importance of combining geometric probes in cosmological reconstruction.

**Om-diagnostic parameter**

Fig. 7 (see Appendix) presents the behaviour of the $Om(z)$ diagnostic as a function of redshift for both the CC and the combined CC+BAO datasets. The $Om(z)$ diagnostic, defined purely from the Hubble parameter, acts as a powerful tool for distinguishing various DE models from the standard $\Lambda$CDM scenario. Since it depends only on the expansion rate, $Om(z)$ provides a model-independent probe of cosmic acceleration and is especially useful for identifying the redshift evolution of the effective DE EoS. The $Om(z)$ diagnostic is sensitive to how the expansion rate evolves with redshift and is capable of differentiating between constant, phantom, and dynamical DE models:

- *Constant positive $Om(z)$ (Cosmological Constant):* If $Om(z)$ remains nearly constant over the redshift range, it indicates that the DE density does not evolve with time. This corresponds to the $\Lambda$CDM model with a constant EoS parameter $\omega = -1$. For $\Lambda$CDM, $Om(z)$ should remain equal to the current matter density parameter $\Omega_{m0}$.
- *Decreasing $Om(z)$ with redshift (Phantom DE):* A decreasing trend in $Om(z)$ indicates that the effective DE EoS lies in the phantom region ($\omega < -1$). In phantom models, the DE density increases as the Universe expands, leading to enhanced late-time acceleration and the possibility of a future cosmic singularity (Big Rip). A downward bending in the $Om(z)$ curve is the hallmark of such behaviour.
- *Increasing $Om(z)$ with redshift (Quintessence or Dynamical DE):* If $Om(z)$ increases with redshift, this corresponds to a quintessence-like DE with $-1 < \omega < -\frac{1}{3}$. In such models, DE density gradually decreases as the Universe expands, yielding a milder acceleration than the cosmological constant and possibly allowing a future return to decelerated expansion.

The $Om(z)$-diagnostic parameter is defined in terms of the Hubble parameter $H(z)$ as

$$Om(z) = \frac{h^2(z) - 1}{(1+z)^3 - 1} = \frac{\left[\frac{1-c_2(1+z)^{n+3}}{1-c_2}\right]^2 - 1}{(z+1)^3 - 1},$$

where $h(z) = H(z)/H_0$ and $H_0$ is the present value of the Hubble parameter. In both CC and CC+BAO panels, the $Om(z)$ curves display a distinctly decreasing behaviour with redshift. Beginning at high values near $z \approx -1$, the $Om(z)$ function consistently declines as the redshift increases toward $z \approx 3$. This downward evolution signals a clear deviation from the constant-$Om$ prediction of $\Lambda$CDM and strongly suggests that the model exhibits phantom-like DE behaviour. The two $Om(z)$ curves in each panel represent the allowed parameter variations obtained from the MCMC analysis. Their smooth and monotonic decline across the entire redshift range further confirms that the effective DE component behaves as a phantom fluid in this model. Moreover, the CC-only reconstruction (left panel) shows a steeper decline, indicating a more pronounced phantom nature. When BAO data are included (right panel), the curves become closer together and the descent is slightly less steep, reflecting the stronger constraints provided by BAO measurements. In all such scenarios, the phantom behaviour leads to stronger late-time acceleration than $\Lambda$CDM, consistent with the decreasing $Om(z)$ trajectories observed. The $Om(z)$ diagnostic complements previous analyses such as the deceleration parameter $q(z)$ and the statefinder diagnostics $(r, s)$ and $(r, q)$ plane analysis. Thus, the $Om(z)$ diagnostic reinforces the conclusion that the underlying cosmological model favours a phantom-like or strongly dynamical DE regime.

**EoS parameter**

The EoS parameter $\omega(z)$ provides a direct relation between the pressure $(p)$ and energy density $(\rho)$ of the cosmic fluid through the expression

$$\omega = \frac{p}{\rho}.$$

It characterizes different phases of cosmic evolution:

- $\omega = 1$ corresponds to stiff fluid,
- $\omega = \frac{1}{3}$ corresponds to radiation,
- $\omega = 0$ corresponds to dust (matter-dominated epoch),
- $-1 < \omega < -\frac{1}{3}$ corresponds to quintessence,
- $\omega = -1$ corresponds to the cosmological constant ($\Lambda$CDM),
- $\omega < -1$ corresponds to phantom DE,
- oscillatory crossing between $\omega > -1$ and $\omega < -1$ indicates quintom behaviour.

Thus, the redshift variation of $\omega(z)$ directly reflects whether DE is constant, dynamical, or phantom-like, and influences the transition from decelerated to accelerated expansion.

The EoS parameters of model-1 and model-2 are presented in Eqs. (26) and (29), respectively. Figs. 8 and 9 (see Appendix) illustrate the redshift evolution of the EoS parameter for two variants of the KHDE models: Model-1 with the Hubble cutoff and Model-2 with the GO cutoff. The behaviour is shown for three different values of the model parameter $c$ and for both CC and CC+BAO datasets. The EoS parameter plays a crucial role in understanding the dynamical nature of DE and its influence on the cosmic expansion history.

For Model-1, the behaviour of $\omega_{de}(z)$ shows notable dependence on the parameter $c$ and the dataset used. For lower values of $c$ (e.g., $c = 0.16$), the EoS parameter tends to lie well below $-1$ at both low and high redshifts, indicating strong phantom behaviour. For $c = 0.19$, the evolution begins in the quintessence region and at low redshift gradually decreases towards $-1$, suggesting a $\Lambda CDM$ model. For $c = 0.22$, the EoS decreases further and approaches the quintessence region at late times ($-1 < \omega < -1/3$), particularly under the CC dataset. The CC+BAO dataset constrains the EoS curves more tightly and leads to smoother evolution, pushing all trajectories closer to $\omega \approx -1$ at low redshift. This indicates that Model-1 tends to approximate $\Lambda$CDM behaviour in the presence of BAO constraints at present epoch, although phantom behaviour persists at higher redshifts.

Model-2 exhibits a qualitatively similar trend but compared to model-1, the EoS curves in model-2 rise more gradually, indicating a weaker phantom effect at early times. The GO cutoff, containing both $H^2$ and $\dot{H}$ terms, effectively regulates the divergence of $\omega(z)$ and yields a more stable evolution than the Hubble cutoff case. Both models enter the phantom regime at low redshifts for lower $c$ values. As redshift decreases, the EoS approaches $-1$, indicating a late-time convergence toward $\Lambda$-like behaviour. This behaviour becomes particularly clear in the CC+BAO reconstructions. For higher $c$, the EoS rises into the quintessence regime at late times in CC-only data. For CC+BAO, however, the curves remain very close to $\omega_{de} = -1$. In a few trajectories, the EoS crosses the $\omega_{de} = -1$ boundary, exhibiting a quintom behaviour. Such behaviour allows a smooth transition from quintessence to phantom.

In summary, the evolution of the EoS parameter in both KHDE models show strong dynamical features, with quintessence-like behaviour at early times and a gradual approach toward $\Lambda$-like behaviour at present epoch. Model-2 with the GO cutoff provides a smoother and more observationally consistent EoS evolution, while Model–1 permits a wider range of phantom and quintom behaviour depending on the value of $c$ and the dataset used.

### $\omega_{de} - \omega'_{de}$ Plane

The $\omega_{de} - \omega'_{de}$ plane is a powerful diagnostic tool first introduced by Caldwell and Linder (2005), allowing a clear classification of DE dynamics into "thawing" and "freezing" categories. The $\omega_{de} - \omega'_{de}$ plane divides dynamical DE models into two major evolutionary regimes:

- *Thawing Region:* Defined by $\omega_{de} < 0$ and $\omega'_{de} > 0$. In this regime, the scalar field begins close to a cosmological constant ($\omega_{de} \approx -1$) in the early epoch and gradually evolves away from it as the Universe expands.

– *Freezing Region:* Defined by $\omega_{de} < 0$ and $\omega'_{de} < 0$. Here, the scalar field evolves at early times but gradually slows down as it approaches a cosmological constant state ($\omega_{de} \to -1$), effectively "freezing" at late times.

These two behaviours capture the typical dynamical patterns of quintessence-type scalar fields but can also be extended – qualitatively – to more general DE models, including holographic and modified gravity frameworks.

From Figs. 10 and 11 (see Appendix), the CC dataset (left panel) exhibits rich dynamical behaviour. For different values of the parameter $c$, the trajectories traverse in freezing region. The trajectories lie predominantly in the freezing region. This indicates that the DE component begins in a phantom-like regime ($\omega_{de} < -1$) with $\omega'_{de} < 0$, gradually evolving toward a more stable state near $\omega_{de} \approx -1$. This variety of behaviours demonstrates that the KHDE model with the Hubble cutoff admits freezing phase, depending sensitively on the parameter $c$. When BAO data are included (right panel), the dynamics becomes far more stable. All trajectories exhibit a monotonic rise of $\omega_{de}$ from deep phantom values toward the $\omega_{de} \to -1$ boundary, and $\omega'_{de}$ consistently taking negative values. Thus, model–1 under CC+BAO data lies completely in the freezing regime, indicating strong convergence toward a $\Lambda$CDM-like attractor at late times.

Fig. 11 (see Appendix) shows the corresponding dynamics for model–2. The CC dataset (left panel) again reveals the trajectories show a pronounced phantom-like onset and a movement into the freezing region, similar to model-1. The GO cutoff, however, moderates extreme evolution, avoiding the sharp turning behaviour seen in the Hubble cutoff case. With CC+BAO data (right panel), model-2 exhibits even stronger stability than model-1. Model-2 therefore resides almost entirely within the freezing region, suggesting that the GO cutoff yields a physically more stable and observationally favoured DE evolution.

The dominance of the freezing behaviour in both models (especially with BAO data) indicates that the effective DE behaves like a scalar field approaching a cosmological-constant-like fixed point. The DE component slows down its evolution as the Universe expands. The future evolution tends toward a stable $\omega_{de} \to -1$ attractor. The models avoid severe phantom divergence (e.g., Big Rip scenarios), despite beginning in phantom regimes. In summary, the $\omega_{de} - \omega'_{de}$ analysis shows that both KHDE models favour a freezing dynamical behaviour at late times, especially when BAO data are included. Model-2 offers a particularly well-behaved and observationally consistent evolution, while model-1 allows richer but more sensitive dynamical features depending on the value of $c$. This phase–space behaviour reinforces the conclusion that both models tend toward a $\Lambda$CDM-like attractor in the future, even though they exhibit phantom or mixed quintom characteristics at earlier epochs.

## Square of the sound speed $v_s^2$

Figs. 12 and 13 (see Appendix) display the evolution of the squared sound speed $v_s^2$ as a function of redshift for model-1 (KHDE with Hubble cutoff) and model-2 (KHDE with GO cutoff), respectively. The squared speed of sound is

defined by

$$v_s^2 = \frac{\dot{p}_{de}}{\dot{\rho}_{de}},$$

and serves as an important theoretical diagnostic to assess the stability of DE models under small perturbations. A physically viable DE model is expected to satisfy $v_s^2 > 0$, ensuring that perturbations propagate without leading to imaginary sound speed or exponential instabilities. Conversely, $v_s^2 < 0$ corresponds to classical instability, indicating that the model cannot remain stable against perturbations at that epoch.

From Fig. 12 (see Appendix), the evolution of $v_s^2$ for model-1 shows distinct features depending on the value of the parameter $c$ and the dataset used. $v_s^2$ remains positive throughout the evolution of model. This indicates that the model-1 is stable. Once BAO data are included, the model becomes unstable at late-times. Fig. 13 (see Appendix) presents the corresponding evolution for model-2. The behaviour is qualitatively similar to model-1 but with important differences due to the modified IR cutoff. The $v_s^2$ diagnostic offers several fundamental insights. Both models tend to become fully stable ($v_s^2 > 0$) throughout evolution when CC data are used, matching expectations for observationally favoured DE behaviour. Higher values of the parameter $c$ lead to better stability in both models, suggesting that DE behaves more smoothly as $c$ increases. Model-2 generally outperforms model-1 in achieving stable behavior without requiring fine-tuning. Its stability is robust across datasets. In summary, the squared sound speed analysis shows that both KHDE models can achieve dynamical stability across cosmic evolution. Model-2 with the GO cutoff exhibits superior stability properties, while model-1 may encounter limited instability unless appropriately constrained by observational data. This reinforces the physical viability of the Kaniadakis holographic scenario as a stable DE framework.

**Age of the models**

The age of the Universe is one of the most fundamental quantities in cosmology and provides a crucial diagnostic for assessing the validity of theoretical models. The cosmic age can be derived from the relation between cosmic time $t$ and redshift $z$, given by

$$t_0 - t = \int_0^z \frac{dz'}{(1+z')\,H(z')}, \tag{34}$$

where $t_0$ denotes the present age of the Universe, $H(z)$ is the Hubble parameter as a function of redshift, and $t(z)$ represents the age at redshift $z$. This integral quantifies the elapsed cosmic time from redshift $z$ to the current epoch, thereby encoding the expansion history predicted by the underlying cosmological model.

For the present work, substituting the model-dependent expression for $H(z)$, we obtain the cosmic age relation in analytic form as

$$t_0 - t = \frac{c_2 - 1}{(n+3)H_0} \ln\left[\frac{1 - c_2(1+z)^{n+3}}{(1-c_2)(1+z)^{n+3}}\right]. \tag{35}$$

This expression encapsulates the time evolution implied by the model and allows direct comparison with observational bounds on the age of the Universe.

Figs. 14 and 15 (see Appendix) depict two important cosmic time diagnostics used to study the age of the Universe within our proposed models: (i) the cosmic time difference $t_0 - t(z)$, and (ii) the cosmic time function $t(z)$ itself. These quantities are essential for evaluating whether the model produces a realistic cosmic chronology that is consistent with current observational estimates of the age of the Universe.

Fig. 14 (see Appendix) illustrates the evolution of the cosmic time difference $t_0 - t(z)$ as a function of redshift for both CC and CC+BAO datasets. This function measures the amount of time elapsed between an earlier cosmic epoch at redshift $z$ and the present epoch at $z = 0$. A larger value of $t_0 - t(z)$ at high redshift indicates that the Universe has spent more time reaching its current state, while the shape of the curve reflects the expansion history controlled by the DE model. The behaviour seen in Fig. 14 (see Appendix) shows that both panels (CC and CC+BAO) reveal a rapid increase in $t_0 - t(z)$ for small values of $z$, indicating that most of the cosmic time is accumulated at late epochs when DE dominates. As $z$ increases, the curves flatten, showing that the early Universe evolves more rapidly and contributes a smaller fraction of the total cosmic age. The CC+BAO reconstruction yields slightly narrower uncertainty bands, reflecting the improved precision of $H(z)$ when BAO constraints are included. This behaviour is consistent with a Universe undergoing late-time acceleration – most of the age is accumulated in the DE-dominated era, whereas only a small fraction corresponds to very early cosmic epochs.

Fig. 15 (see Appendix) shows the direct cosmic time function $t(z)$, which gives the age of the Universe at redshift $z$. The value at $z = 0$ gives the current age of the Universe predicted by the model. The marked red points in Fig. 13 indicate: $t_0^{(\mathrm{CC})} \approx 0.01404 \times 9.78$ Gyr $\approx 13.73$ Gyr, $t_0^{(\mathrm{CC+BAO})} \approx 0.01420 \times 9.78$ Gyr $\approx 13.89$ Gyr. These values lie very close to the Planck 2018 estimate for the age of the Universe: $t_0^{\mathrm{Planck}} = 13.80 \pm 0.02$ Gyr. Thus, both CC and CC+BAO datasets produce fully consistent cosmic age predictions. The CC+BAO value is particularly noteworthy since it matches the Planck result to within observational uncertainties. The narrow uncertainty band in the CC+BAO panel demonstrates that BAO data significantly reduce uncertainties in the late-time expansion rate, allowing a precise determination of the cosmic age.

In summary, the analysis of cosmic time evolution demonstrates that the proposed KHDE models yield realistic and observationally consistent predictions for the age of the Universe. Both models produce ages in agreement with Planck measurements, with improved precision under CC+BAO constraints. The smooth and physically plausible behaviour of $t(z)$ and $t_0 - t(z)$ further confirms the viability of the models in describing the cosmic expansion history.

## Cosmic coincidence

One of the long-standing puzzles in modern cosmology is the cosmic coincidence problem, which asks why the energy densities of DE and matter happen to be of the same order of magnitude in the current epoch, despite their

markedly different evolutionary behaviors. To characterize this issue, the coincidence parameter $\bar{r}$ is introduced as

$$\bar{r} = \frac{\rho_m}{\rho_{de}},$$

where $\rho_m$ and $\rho_{de}$ denote the energy densities of matter and DE, respectively. This parameter measures the relative dominance of these two major cosmic components and provides insight into their mutual evolution or possible interactions. Within the standard $\Lambda$CDM framework, $\bar{r}$ decreases rapidly over time, since the matter density scales as $\rho_m \propto a^{-3}$, while the DE density remains constant owing to the equation-of-state value $\omega_{de} = -1$. In contrast, models involving dynamical DE or modified gravity can yield a more moderate evolution of $\bar{r}$, thereby offering a potential resolution to the coincidence problem.

Fig. 16 (see Appendix) presents the evolution of the coincidence parameter $\bar{r}$ as a function of redshift for both model-1 (KHDE with Hubble cutoff) and model-2 (KHDE with GO cutoff). Both models exhibit the same qualitative behaviour, with some quantitative differences. At high redshift ($z \gtrsim 2$), $\bar{r}(z)$ approaches $\sim 1.6 - 1.7$, indicating strong matter domination. As redshift decreases, $\bar{r}(z)$ falls rapidly, approaching values close to unity at $z \to -0.5$ (future epoch), consistent with DE becoming dominant. This behaviour reflects the expected background evolution: matter scales as $(1+z)^3$, while HDE evolves more slowly. The rapid decline of $\bar{r}$ from high to low redshift confirms that DE becomes increasingly dominant as the Universe expands. The coincidence parameter for both models is reconstructed using CC-only data and the combined CC+BAO datasets. CC-only curves (dashed lines) show slightly higher values of $\bar{r}$ at intermediate redshifts, reflecting greater uncertainty in DE evolution when only CC data are used. CC+BAO curves (solid lines) lie lower at early times but converge with CC predictions at later times. This indicates that BAO data refine the estimation of DE dynamics, leading to a more reliable prediction of the ratio $\rho_m/\rho_{de}$.

In summary, the coincidence parameter analysis shows that both KHDE models exhibit realistic matter–DE evolution. They do not entirely solve the cosmic coincidence problem but significantly moderate it, particularly under CC+BAO constraints and in the case model-2. This behaviour enhances the physical viability of the models compared to standard DE scenarios.

## Thermodynamics and entropy

We now turn to the thermodynamic aspects of the models by analyzing the entropy density $\mathcal{S}$ and the temperature $\mathcal{T}$ of the cosmic fluid as functions of redshift $z$ (see Figs. 17(a) and 17(b) (see Appendix)). According to the second law of thermodynamics, the entropy associated with the cosmic horizon – both within the horizon volume and on its boundary – must remain non-negative and increase monotonically with cosmic time. When the first and second laws are simultaneously applied to a comoving volume $V$, the fundamental thermodynamic relation takes the form (Myung 2011)

$$\mathcal{T}\, d\mathcal{S} = d(\rho V) + p\, dV = d[(\rho + p)V] - V\, dp, \tag{36}$$

where $p$ is the total pressure, $\rho = \rho_m + \rho_{de}$ is the total energy density, and $\mathcal{T}$ and $\mathcal{S}$ denote the temperature and entropy, respectively. For a perfect fluid, the thermodynamic relation connecting pressure (or energy density) with temperature is

$$dp = \left(\frac{\rho + p}{\mathcal{T}}\right) d\mathcal{T}. \tag{37}$$

Substituting Eq. (37) into Eq. (36), we obtain

$$d\mathcal{S} = \mathcal{T}^{-1} d[(\rho + p)V] - (\rho + p)V\,\mathcal{T}^{-2} d\mathcal{T} = d\left[\frac{(\rho + p)V}{\mathcal{T}} + c_i\right], \tag{38}$$

$$\Rightarrow \qquad \mathcal{S} = \frac{(\rho + p)V}{\mathcal{T}}, \tag{39}$$

where $c_i$ is an integration constant. For an adiabatic process ($\mathcal{S}$ = constant), the same form of entropy follows directly from the conservation law, rewritten as $d[(\rho + p)V] = V\,dp$. Defining the entropy density $\overline{\mathcal{S}}$ as the entropy per unit comoving volume, we find

$$\overline{\mathcal{S}} = \frac{\mathcal{S}}{V} = \frac{\rho + p}{\mathcal{T}} = \frac{(1 + \gamma)\rho}{\mathcal{T}}, \tag{40}$$

where $0 < \gamma < 1$ is the equation-of-state (EoS) parameter. To express the entropy density explicitly as a function of temperature, we recast the first law of thermodynamics as

$$d(\rho V) + \gamma\rho\, dV = (1 + \gamma)\mathcal{T}\, d\left(\frac{\rho V}{\mathcal{T}}\right). \tag{41}$$

After straightforward algebraic manipulations, we obtain the following compact expressions for the entropy density and temperature:

$$\overline{\mathcal{S}} = (1 + \gamma)\,\rho^{\,1/\gamma}, \tag{42}$$

$$\mathcal{T} = \rho^{\,\gamma/(1+\gamma)}. \tag{43}$$

Finally, substituting the energy density $\rho$ from Eqs. (8)–(10), the metric potentials in Eq. (14), and the scalar field in Eq. (16), we obtain the redshift-dependent expressions for the entropy density and temperature of all the cosmological models studied in this work. Since these expressions are very lengthy, we do not present them explicitly and instead show their physical behaviour using graphs.

Odintsov and Paul (2023) proposed a non-singular five-parameter entropy function that generalizes several well-known entropy formulations and remains regular throughout the entire cosmic evolution. This feature allows for a consistent description of bounce cosmology, in which the Universe smoothly evolves from a contracting phase to an expanding one. Similarly, Nojiri et al. (2022c)

presented a unified, non-singular cosmological scenario within the framework of ghost-free $f(R, G)$ gravity, where $R$ and $G$ denote the Ricci and Gauss–Bonnet scalars, respectively. Figure 17 (see Appendix) shows the redshift evolution of the temperature $\mathcal{T}(z)$ and entropy density $\mathcal{S}(z)$ for the two KHDE models considered. Both quantities increase with redshift, reflecting the hotter and denser conditions of the early Universe. At low redshifts, $\mathcal{T}(z)$ and $\mathcal{S}(z)$ flatten or decrease as cosmic expansion proceeds and dark energy becomes dominant. This behaviour is physically expected in an expanding Universe and supports the thermodynamic viability of the KHDE models, as well as their consistency with the generalized second law of thermodynamics.

The left panel of Fig. 17 (see Appendix) displays the evolution of the temperature $\mathcal{T}(z)$ for model-1 and model-2 using CC and CC+BAO constraints. In both cases, $\mathcal{T}(z)$ increases monotonically with redshift, indicating hotter conditions in the early Universe. The CC+BAO curves lie slightly below the CC-only results at higher redshifts, suggesting a more moderate thermal evolution when BAO data constrain the expansion history. The right panel shows the entropy density $\mathcal{S}(z)$, which rises rapidly at early times due to higher energy density. Model-2 yields slightly larger intermediate-redshift values because of the GO cutoff contribution. However, under CC+BAO constraints, both models closely converge, demonstrating that BAO data significantly tighten the thermal evolution and reduce model differences.

In conclusion, the temperature and entropy density evolution in Fig. 17 (see Appendix) reinforce the physical plausibility and thermodynamic consistency of both KHDE models. Their behaviour fits well within the expected thermal history of the Universe and supports their viability as competing scenarios to explain late-time cosmic acceleration. Moreover, the continuous decrease in temperature with time corresponds to the expected cooling of the universe as it expands (Singh and Singh 2018; Aditya et al. 2025).

## 5 Conclusion

In this work, we have carried out a comprehensive cosmological and physical analysis of two variants of the KHDE models (Model-1 with the Hubble horizon cutoff and Model-2 with the GO cutoff) using the latest CC and the combined CC+BAO observational datasets. A wide range of cosmological diagnostics, dynamical tools, and thermodynamic parameters were employed to test the viability, stability, and observational consistency of the models. The combined interpretation of all these analyses leads to the following conclusions.

– Both models successfully reproduce the late-time accelerated expansion of the Universe. The reconstructed EoS parameter $\omega_{de}(z)$ exhibits phantom or quintom-like behaviour at early epochs, with a smooth evolution toward $\omega_{de} \to -1$ at the present epoch. Model-2, due to the GO cutoff, presents a more controlled and stable evolution of $\omega_{de}$, while Model-1 shows a richer dynamical structure that depends sensitively on the parameter $c$. Inclusion of BAO data further tightens the constraints and drives both models closer to $\Lambda$CDM at low redshift. The current values of EoS parameter in our models are in good agreement with the modern observational data derived from WMAP9, $H_0$, SNe Ia, CMB, and BAO observations as $\omega_0 = -1.084 \pm 0.063$ (Hinshaw et al. 2013), this was refined to $\omega_0 = -1.006 \pm 0.0451$ in 2015 (Ade

et al. 2015) and further to $\omega_0 = -1.028 \pm 0.032$ in 2018 (Aghanim et al. 2020). The $\omega_{de}-\omega'_{de}$ analysis further demonstrates that the models predominantly occupy the freezing regime, indicating that DE evolves toward a stable cosmological-constant-like attractor. Model-2 displays smoother trajectories, emphasizing its dynamical robustness. The squared sound speed $v_s^2$ shows that both models can remain classically stable ($v_s^2 > 0$) throughout most of the cosmic history. The GO cutoff (Model-2) yields more stable behaviour across redshifts, reinforcing its thermodynamical and perturbative consistency, whereas Model-1 and 2 exhibits low-redshift instabilities under CC+BAO only constraints.

- The behaviour of the deceleration parameter $q(z)$ provides strong evidence for the viability of our models. The reconstructed evolution clearly shows that the Universe experiences an early decelerated phase ($q > 0$), dominated by matter, followed by a transition into the presently observed accelerated phase ($q < 0$). The transition redshift obtained from our analysis lies in the range $z_t \simeq 0.5-0.7$, which is fully consistent with recent observational estimates from SNe Ia, CC, and BAO data. The smooth evolution toward $q \to -1$ at late times demonstrates that both KHDE models naturally approach a de Sitter-like phase, further reinforcing their compatibility with the observed expansion history of the Universe. The statefinder pairs $(r, s)$ and $(r, q)$ confirm that both models evolve from matter-dominated states toward the $\Lambda$CDM fixed point $(r, s) = (1, 0)$ at late times. The trajectories lie in the quintessence and phantom regions at earlier epochs, reflecting the dynamical nature of KHDE. The $Om$-diagnostic reveals a consistently decreasing $Om(z)$ behaviour, indicating that the KHDE energy component behaves predominantly like phantom DE rather than $\Lambda$CDM. This phantom-like evolution is mild and smooth, without leading to destructive divergences in other cosmological functions.
- The predicted ages of the Universe, obtained from the cosmic time functions $t(z)$ and $t_0 - t(z)$, lie between 13.7 and 13.9 Gyr, in excellent agreement with the Planck 2018 result. The coincidence parameter $\bar{r}(z)$ evolves smoothly from large values at early times (matter domination) to near-unity values today (DE domination). Although neither model fully resolves the coincidence problem, both significantly alleviate it through mild tracking behaviour. Model-2 exhibits a slightly better performance due to the smoother DE evolution induced by the GO cutoff. The entropy density and temperature of the KHDE fluid follow the physically expected trends: both increase with redshift, reflecting hotter and denser early epochs. Entropy density exhibits a peak behaviour linked to the transition toward DE dominance, while remaining consistent with the generalized second law of thermodynamics. Both models, particularly with BAO constraints, demonstrate full thermodynamic viability.

Our results show that the KHDE framework provides a physically consistent, observationally viable, and dynamically rich alternative to the $\Lambda$CDM paradigm. Model-2, incorporating the GO cutoff, emerges as the more stable and better constrained scenario, offering smoother evolution in all diagnostics. Model-1, though more dynamically flexible, also remains compatible with current data and exhibits interesting quintom and phantom behaviours. Both models satisfy thermodynamic requirements, predict realistic cosmic ages, and

display stable dynamical evolution. In conclusion, the combination of observational constraints and a wide spectrum of physical diagnostics demonstrates that KHDE with the GO cutoff constitutes a promising route for describing the late-time acceleration of the Universe.

**Acknowledgment:** The work has been supported financially by National Board for Higher Mathematics, Department of Atomic Energy, Govt. of India under the Research project No.: 02011/8/2023 NBHM(R.P.)/R & D II/3073.

## References

Abreu, E. M., et al., 2018, *EPL 124, 30003.*
Ade, P. A. R., et al., 2016, *Astron. Astrophys. 594, A13.*
Adhav, K. S., 2011, *Int. J. Astron. Astrophys. 1, 204.*
Aditya, Y., 2024, *Bulg. Astron. J. 40, 95.*
Aditya, Y., 2025, *Bulg. Astron. J. 43, 15.*
Aditya, Y., D. R. K. Reddy, 2018a, *Int. J. Geom. Theor. Mod. Phys. 15(9), 1850156.*
Aditya, Y., D. R. K. Reddy, 2018b, *Astrophys. Space Sci. 363, 207.*
Aditya, Y., D. R. K. Reddy, 2018c, *Eur. Phys. J. C 78, 619.*
Aditya, Y., et al., 2019, *Eur. Phys. J. C 79, 1020.*
Aditya, Y., et al., 2020, *Indian J. Phys. 95, 383.*
Aditya, Y., et al., 2021, *New Astron. 84, 101504.*
Aditya, Y., et al., 2022, *Int. J. Mod. Phys. A 37, 2250107.*
Aditya, Y., et al., 2025, *Afr. Mat. 36, 120.*
Aghanim, N., et al., 2020, *Astron. Astrophys. 641, A6.*
Akarsu, O., Kilinc, C. B., 2010, *Gen. Relativ. Gravit. 42, 119.*
Ali, S., et al., 2024, *New Astron. 110, 102226.*
Batista, C. E. M., et al., 2012, *Phys. Rev. D 85, 084008.*
Bhaskara Rao, M. P. V. V., et al., 2021, *Int. J. Mod. Phys. A 36, 2150260.*
Brans, C., Dicke, R. H., 1961, *Phys. Rev. 124, 925.*
Caldwell, R., Kamionkowski, M., Weinberg, N., 2003, *Phys. Rev. Lett. 91, 071301.*
Caldwell, R., Linder, E. V., 2005, *Phys. Rev. Lett. 95, 141301.*
Capozziello, S., 2002, *Int. J. Mod. Phys. D 11, 483.*
Carames, T. R. P., et al., 2014, *Eur. Phys. J. C 74, 3145.*
Chirde, V. R., Shekh, S. H., 2018, *Indian J. Phys. (DOI:10.1007/s12648-018-1236-y).*
Collins, C. B., et al., 1980, *Gen. Relativ. Gravit. 12, 805.*
Copeland, E. J., et al., 2006, *Int. J. Mod. Phys. D 15, 1753.*
De Moraes, W. A. G., Santos, A. F., 2019, *Gen. Relativ. Gravit. 51, 167.*
Drepanou, N., et al., 2022, *Eur. Phys. J. C 82, 449.*
Ford, L. H., 1987, *Phys. Rev. D 35, 2955.*
Ghaffari, S., 2022, *Mod. Phys. Lett. A 37, 2250152.*
Gibbons, G. W., Hawking, S. W., 1977, *Phys. Rev. D 15, 2738.*
Granda, L. N., Oliveros, A., 2008, *Phys. Lett. B 669, 275.*
Granda, L. N., Oliveros, A., 2009, *Phys. Lett. B 671, 199.*
Hassan, Z., Mandal, S., Sahoo, P. K., 2021, *Fortschr. Phys. 69, 2100023.*
Hawking, S. W., 1975, *Commun. Math. Phys. 43, 199.*
Hinshaw, G., et al., 2009, *Astrophys. J. Suppl. Ser. 180, 225.*
Hinshaw, G., et al., 2013, *Astrophys. J. Suppl. Ser. 208, 19.*
Hooft, G. 't., 1993, *arXiv:gr-qc/9310026.*
Jahromi, A. S., et al., 2018, *Phys. Lett. B 780, 21.*
Jawad, A., Sultan, A. M., 2021, *Adv. High Energy Phys. 2021, 5519028.*
Johri, V. B., Sudharsan, R., 1989, *Aust. J. Phys. 42, 215.*
Johri, V. B., Desikan, K., 1994, *Gen. Relativ. Gravit. 26, 1217.*
Joyce, A., Jain, B., Khoury, J., Trodden, M., 2015, *Phys. Rept. 568, 1.*
Kaniadakis, G., 2001, *Physica A 296, 405.*
Kaniadakis, G., 2002, *Phys. Rev. E 66, 056125.*
Kantowski, R., Sachs, R. K., 1966, *J. Math. Phys. 7, 433.*
Kristian, J., Sachs, R. K., 1966, *Astrophys. J. 143, 379.*
Li, M., 2004, *Phys. Lett. B 603, 1–5.*

Masi, M., 2005, *Phys. Lett. A 338, 217.*
Mishra, S. S., 2024, *Astrophys. J. 970, 57.*
Moradpour, H., et al., 2018, *Eur. Phys. J. C 78, 829.*
Moradpour, H., et al., 2020, *Eur. Phys. J. C 80, 732.*
Moresco, M., 2015, *Mon. Not. R. Astron. Soc. 450, L16.*
Moresco, M., et al., 2012, *J. Cosmol. Astropart. Phys. 08, 006.*
Moresco, M., et al., 2016, *J. Cosmol. Astropart. Phys. 05, 014.*
Murali, K., et al., 2024, *Mod. Phys. Lett. A 39, 2450106.*
Murali, K., et al., 2025, *AIP Conf. Proc. 3298, 040022.*
Myung, Y. S., 2011, *Astrophys. Space Sci. 335, 2.*
Naidu, K. D., et al., 2021, *Mod. Phys. Lett. A 36, 2150054.*
Nojiri, S., Odintsov, S. D., 2006, *Gen. Relativ. Gravit. 38, 1285–1304.*
Nojiri, S., et al., 2019, *Phys. Lett. B 797, 134829.*
Nojiri, S., et al., 2020, *Phys. Rev. D 102, 023540.*
Nojiri, S., et al., 2021, *Symmetry 13, 928.*
Nojiri, S., et al., 2022a, *Astrophysics 65, 534–551.*
Nojiri, S., et al., 2022b, *Phys. Rev. D 105, 044042.*
Nojiri, S., et al., 2022c, *Phys. Dark Univ. 35, 100984.*
Nojiri, S., et al., 2024, *Universe 10, 352.*
Odintsov, S. D., Paul, T., 2023, *Phys. Dark Univ. 39, 101159.*
Pavon, D., Zimdahl, W., 2005, *Phys. Lett. B 628, 206–210.*
Perlmutter, S., et al., 1998, *Nature 391, 51.*
Prasanthi, U. Y. D., Aditya, Y., 2020, *Results Phys. 17, 103101.*
Prasanthi, U. Y. D., Aditya, Y., 2021, *Phys. Dark Univ. 31, 100782.*
Prasanthi, A. V., et al., 2024, *East Eur. J. Phys. 2, 10.*
Raju, K. D., et al., 2020a, *Astrophys. Space Sci. 365, 45.*
Raju, K. D., et al., 2020b, *Astrophys. Space Sci. 365, 28.*
Rana, D. S., et al., 2025, *Universe 11, 242.*
Rao, B. G., et al., 2024, *East Eur. J. Phys. 1, 43.*
Rastall, P., 1972, *Phys. Rev. D 6, 3357.*
Riess, A. G., et al., 1998, *Astron. J. 116, 1009.*
Sadeghi, J., et al., 2023, *Mod. Phys. Lett. A 38, 2350076.*
Santhi, M. V., et al., 2016, *Can. J. Phys. 94, 578.*
Santhi, M. V., et al., 2018, *Int. J. Geom. Methods Mod. Phys. 15, 1850161.*
Santhi, M. V., Chinnappalanaidu, T., 2023, *Astrophys. Space Sci. 368, 1–17.*
Sharif, M., Zubair, M., 2010, *Astrophys. Space Sci. 330, 399.*
Sharma, U. K., et al., 2022, *Int. J. Mod. Phys. D 31, 2250013.*
Singh, A., Singh, G. P., Pradhan, A., 2022, *Int. J. Mod. Phys. A 37, 2250104.*
Singh, A., Pradhan, A., 2023, *Indian J. Phys. 97, 631.*
Singh, M. S., Singh, S. S., 2018, *Turk. J. Phys. 42, 198.*
Spergel, D., et al., 2003, *Astrophys. J. Suppl. Ser. 148, 175–194.*
Steinhardt, P., Wang, L., Zlatev, I., 1999, *Phys. Rev. D 59, 123504.*
Tavayef, M., et al., 2018, *Phys. Lett. B 781, 195.*
Thorne, K. S., 1967, *Astrophys. J. 148, 51.*
Tsallis, C., Cirto, L. J. L., 2013, *Eur. Phys. J. C 73, 2487.*
Verde, L., et al., 2002, *Mon. Not. R. Astron. Soc. 335, 432–440.*
Visser, M., 2018, *Phys. Lett. B 782, 83.*
Wang, S., et al., 2017, *Phys. Rep. 696, 1–57.*
Zlatev, I., Wang, L., Steinhardt, P., 1999, *Phys. Rev. Lett. 82, 896–899.*